Acta Pharmaceutica Sinica B 2026;16(3):1696−1716

Chinese Pharmaceutical Association
Institute of Materia Medica, Chinese Academy of Medical Sciences

Acta Pharmaceutica Sinica B

www.elsevier.com/locate/apsb
www.sciencedirect.com

ORIGINAL ARTICLE

Extracellular vesicles-derived hybrid biomimetic nanoplatforms camouflaged Golgi apparatus-targeted aggregation induced emission photosensitizer to elicit pyroptosis and immunogenic cell death for efficient antitumor photoimmunotherapy

Xing Zhao, Xi Wu, Ranran Shang, Haitao Dou, Huachao Chen*, Ninghua Tan*

State Key Laboratory of Natural Medicines, School of Traditional Chinese Pharmacy, China Pharmaceutical University, Nanjing 211198, China

Received 4 May 2025; received in revised form 20 July 2025; accepted 28 September 2025

KEY WORDS

Aggregation-induced emission;
Golgi apparatus-targeted;
Biomimetic hybrid nanoplatforms;
Photodynamic therapy;
Pyroptosis;
Immunogenic cell death;
Photoimmunotherapy

Abstract Pyroptosis is a unique programmed cell death pattern, and targeting it is an effective strategy against cancer therapy by overcoming apoptosis resistance. However, Golgi apparatus-targeted aggregation induced emission (AIE) photosensitizer as pyroptosis inducer for efficient antitumor treatment has not been reported. In this study, we successfully synthesized three new AIEgens, including TMN, TBN and TCN, by changing functional groups through a reasonable molecular design strategy, which targeted mitochondria, lysosome and Golgi apparatus (GA), respectively. *In vitro* experiments demonstrated that TCN exhibited the strongest reactive oxygen species (ROS) production ability and significant phototoxicity. Therefore, TCN as the GA-targeted AIE photosensitizer wore biomimetic hybrid extracellular vehicles (EVs) and M1-type macrophage membranes (denoted as EM@TCN) as pyroptosis inducer were rationally designed and engineered to trigger the production of GA cytotoxic ROS *in situ*. EM@TCN plus white light irradiation caused GA oxidative stress and induced pyroptosis synergistic photoimmunotherapeutic, which could rebuild tumor microenvironment and improve tumor immunogenicity. Combined with αPD-L1 (anti-mouse PD-L1 antibody), the biomimetic hybrid delivery system

*Corresponding authors.
E-mail addresses: nhtan@cpu.edu.cn (Ninghua Tan), huachao.chen@cpu.edu.cn (Huachao Chen).

Peer review under the responsibility of Chinese Pharmaceutical Association and Institute of Materia Medica, Chinese Academy of Medical Sciences.

https://doi.org/10.1016/j.apsb.2025.11.010

EM@TCN significantly inhibit the both primary and distant tumors, and effectively suppress the orthotopic breast tumor. This is the first report on a hybrid nanovesicle coated GA-targeted AIE photosensitizer to induce pyroptosis for combination with αPD-L1 to enhance antitumor photoimmunotherapy.

1. Introduction

Immunotherapy, especially immune checkpoint blockade (ICB) therapy has achieved remarkable therapeutic outcomes in the clinical against various malignant tumors[1-4]. However, insufficient tumor immunogenicity and immunosuppressive tumor microenvironment (TME) severely limit its application[5,6]. Previous studies have revealed that initiation of antigen processing cells, increase the infiltration of cytotoxic T lymphocytes and reverse the immunosuppressive TME can induce stronger antitumor immune response, thereby improving ICB efficiency[7]. Nowadays, induction of immunogenic cell death (ICD) in tumor synergized with ICB therapy is greatly accepted to optimize the performance of cancer immunotherapy. ICD, like pyroptosis, an inflammatory programmed cell death (PCD) pattern, which is performed by the activation gasdermin family (GSDMs) and caspases, characterized by cell membrane pore formation, cell swelling with large bubbles, and then fast release of cell contents, resulting in cell death[8-12]. Not only can pyroptosis overcome apoptosis resistance, more importantly, because of membrane ruptures and leakage of cytoplasmic pro-inflammatory cytokines, but also cytotoxic lymphocytes were activated to provoke an antigen-specific immune response and release damage-associated molecular patterns (DMAPs), which further reverse the immunosuppressed state of TME and stimulate a "cold" tumor to be an immunogenic "hot" tumor microenvironment[13-16]. Therefore, pyroptosis can trigger a strong antigen-specific immune response, enhance ICB efficiency, inhibit tumor proliferation, induce immune memory, and prevent tumor metastasis[17]. A series of pyroptosis-induced nanoplatforms have been constructed to regulate the tumor immunosuppressive microenvironment and activate antitumor immune response[18-24]. However, pyroptosis involved in these nanoplatforms is usually affected by chemotherapeutic drugs, whose biomedical applications were restricted because of their drug resistance and severe side effects[25,26]. Therefore, the combination of pyroptosis inducers and immune checkpoint inhibitor (ICI) have been shown to boost the anticancer effect of immunotherapy, which powerfully suppressed the intrinsic immune escape mechanism of tumors and aroused a significant systematic immune response.

Fluorescence imaging-guided photodynamic therapy (PDT) has captivated extensive interest due to its significant advantages of negligible invasiveness, good spatiotemporal selectivity, minimized systemic toxicity and simple operation over conventional therapeutic methods[27-31]. However, most of the traditional photosensitizers (PSs) generally show quenched fluorescence and insufficient singlet oxygen generation in the aggregate state, which makes them less ideal for PDT[32]. To address this aggregation-caused quenching (ACQ) issue, PSs with aggregation-induced emission (AIE) were developed in 2001 by Tang's group, which could emit bright fluorescence and generate abundant ROS in the aggregates[33-35]. This is a consequence of the restriction of intramolecular motions (RIM) and prohibition of non-radiative energy dissipation of AIEgens when they are in an aggregate state[36,37]. Recently, some AIEgens have been used as pyroptosis inducers through massive production of ROS *in situ* at specific subcellular organelles, such as mitochondria and cell membrane, thus lead to the death of cancer cells[38-41]. Among numerous organelles, Golgi apparatus (GA) is a crucial target due to the outstanding therapeutic effect of GA oxidative stress induced by ROS *in situ* during PDT, but AIEgens selectively targeting GA remains a challenge[42-44]. Even more, AIEgens selectively targeting GA induce pyroptosis to boost antitumor immunity haven't been reported. In this regard, it is very intriguing to elaborate subcellular organelles targeted AIEgens of PDT for inducing robustly pyroptosis, activate antitumor immune response and reprogram immunosuppressed TME, achieving powerfully tumor growth inhibition.

Herein, a series of homologous AIEgens, namely TMN, TBN, TCN, were rationally designed and facilely synthesized through slight structural modifications based on the same backbone. These three AIEgens were anchoring to various subcellular organelles including mitochondria, lysosome and Golgi apparatus, respectively. Among them, TCN exhibited superior AIE property and stronger type-II ROS generation efficiency, specific GA targeting ability and excellent photostability *in vitro* studies. To further improve the TCN delivery efficiency, natural-derived nanomaterials like extracellular vesicles (EVs) and M1-type macrophage membranes (MM) are applied to construct the nanocarrier system, owing to their favorable self-targeting homing ability, low immunogenicity, good biocompatibility and prolonged circulation time[45,46]. In addition, it is reported that M1 macrophage membranes could re-educate the tumorigenic M2-type macrophages to tumoricidal M1-type macrophages, demonstrating great potential in remodeling immunosuppressive TME[47]. Thereafter, a hybrid cancer cell-derived nanovesicles (denoted as EM@TCN) composed of 4T1 breast cancers derived EVs and M1-type MM were developed as the carriers of TCN. *In vitro* studies demonstrated that EM@TCN can produce more ROS in GA and exhibited pronounced cell death under white light irradiation, which can be attributed to the activated gasdermin-mediated pyroptosis and ICD process. In addition, *in vivo* experiments also indicated that EM@TCN plus white light illumination could significantly inhibit the proliferation of primary and distant tumors on 4T1 breast bilateral tumor model. At the same time, when combined EM@TCN with ICI (αPD-L1), it can not only suppress orthotopic breast cancer tumor growth, but also inhibit lung metastasis and extend the survival period of metastasis breast cancer mice, demonstrating the enormous potential of enhanced antitumor immunotherapy based on PDT and photoinduced pyroptosis (Scheme 1). This is the first report to design and synthesize hybrid biomimetic nanoplatforms camouflaged Golgi apparatus-targeted AIE photosensitizer (TCN) to induce pyroptosis, arouse antitumor immune response and a series of amplification effects in TME for effectively treating the 4T1 breast cancer model[51].

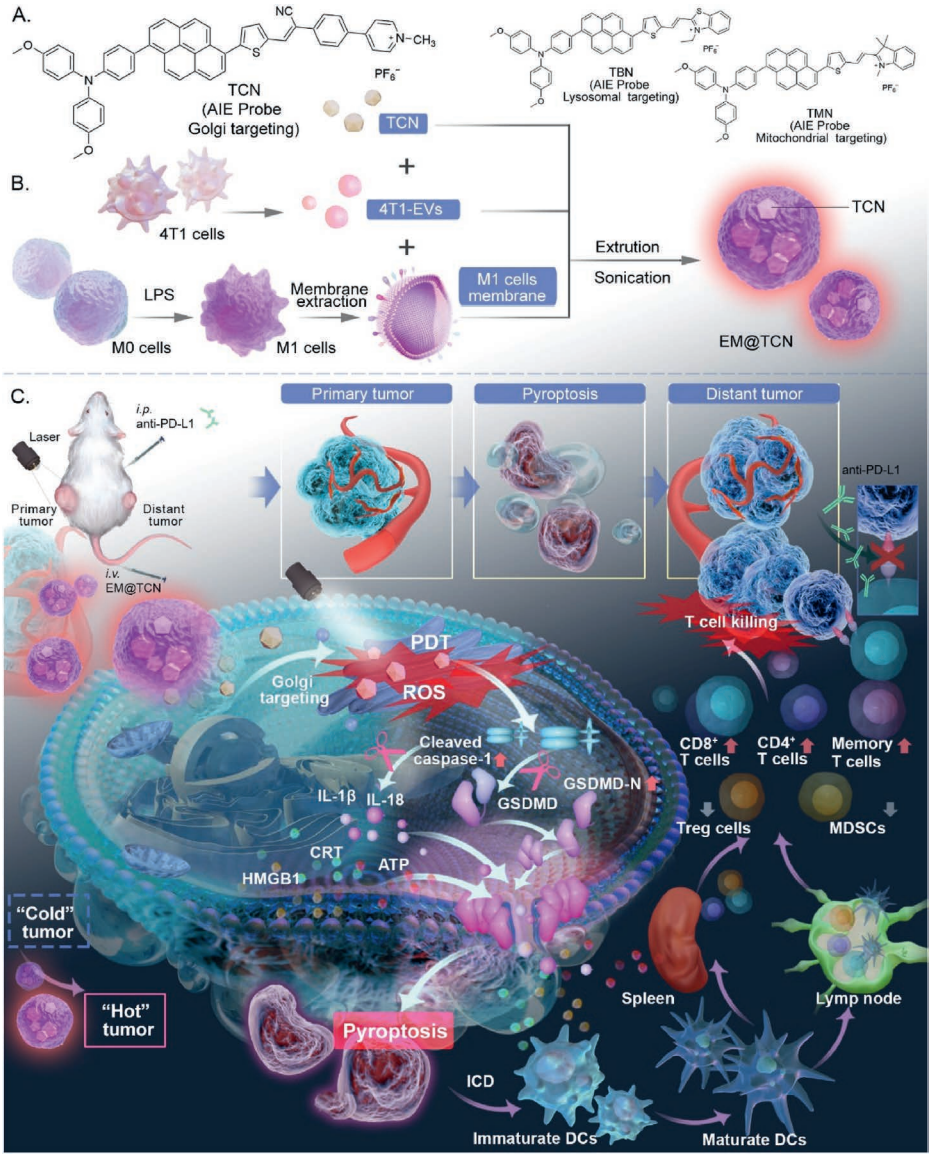

Scheme 1 Schematic illustration of the antitumor mechanism of EM@TCN plus white light irradiation by evoking pyroptosis-mediated photoimmunotherapy. (A) Chemical structures of TMN, TBN and TCN. (B) Preparation of EM@TCN. (C) Golgi apparatus-targeted EM@TCN induced photo-triggered pyroptosis synergistically amplified ICD effects for efficient tumor photoimmunotherapy.

Therefore, this work provides novel perspectives on the rational fabricating the multifunctional hybrid nanovesicles to effectively delivery subcellular-targeted AIE photosensitizers for evoking pyroptosis and antitumor immunity during PDT.

2. Materials and methods

2.1. Materials

All chemical reagents were provided from Bidepharma-Tech, Leyan Chemicals, J&K Chemicals, Sigma−Aldrich or Aladdin Reagents. BCA Protein Quantitative Assay Kit, Reactive Oxygen Species (ROS) Assay Kit, Calcein-AM/PI Cell Viability Assay Kit, JC-1 Assay Kit, ATP Bioluminescent Assay Kit and LDH Cytotoxicity Assay Kit were provided from Beyotime Biotechnology (Shanghai, China). Annexin V Alexa Fluor™ 488/PI Cell Apoptosis Kit, Hoechst 33342, Lyso-Green, Mito-Green and ER-Blue were obtained from Invitrogen (Carlsbad, USA). Golgi-Green was supplied by KeyGEN Biotech Co., Ltd. (Nanjing, China). Antibodies of γ-H_2AX, HMGB1, GM130, GSDMD and GSDME were supplied by Abcam (Cambridge, UK). Antibodies of CD9, CD63, TSG101, CRT, HSP70, Caspase 1, Caspase 3, CD3, CD4 and PD-L1 were supplied by Proteintech (Wuhan, China). CD8 antibody was provided from Servicebio (Wuhan, China). Antibodies of anti-CD45-Elab Fluor® Red 780, anti-CD3-APC, anti-CD4-FITC, anti-CD8-PE, anti-CD44-PE/Cy7, anti-CD62L-Percp/Cy5.5, anti-MHCII-PE, anti-CD11c-PerCP/Cy5.5, anti-CD80-APC, anti-CD86-FITC, anti-CD11b-PE, anti-F4/80-Percp/Cy5.5, anti-CD206-APC, anti-CD25-Elab Fluor® Violet 450 and anti-Gr-1-APC were purchased from Elabscience Co., Ltd. (Houston, USA).

2.2. Methods

All the experimental procedures are given in the Supporting Information.

3. Results and discussions

3.1. Preparation and characterization of EM@TCN

In order to investigate the influence of various electron acceptors with different electron-withdrawing abilities and spatial conformations on the subcellular-organelle-targeting properties of organic phototheranostic agents, three D−π−A structured homologous luminogens with identical donors, same π-bridge, and diverse acceptors, namely TMN, TBN, TCN, were tactfully designed and synthesized. The design of the targeted AIE photosensitizer TCN for the Golgi apparatus mainly relies on the structure of cyanopyridinium salts, which plays an important role in targeting Golgi apparatus. Their chemical structures were shown in Fig. 1A, in which these compounds can be easily synthesized through Suzuki cross-coupling reaction and condensation reaction with high yields. Their synthetic routes were presented in Supporting Information Fig. S1. All key intermediates and target products were elucidated by nuclear magnetic resonance (NMR) spectroscopy and high-resolution mass spectrometry (HR-MS) in Supporting Information Figs. S2−S19. Next, their spectroscopic properties of TMN, TBN and TCN were taken using UV−Vis and fluorescence spectroscopies. As depicted in Fig. 1B, TMN, TBN and TCN showed wide absorption with the main absorption peaks of 409, 473, and 432 nm, respectively. The AIEgens maximum emission wavelengths in toluene were located at 495, 510, and 660 nm, respectively (Fig. 1C). Their absorption wavelength is relatively short, which limits the deep penetration depth into tumors. However, their penetration depth is sufficient for subcutaneous xenograft tumor models in this work. The large Stokes shift (228 nm for TCN) can reduce the interference of biological spontaneous fluorescence and is beneficial to enhance the imaging signal-to-noise ratio. The AIE effects of TMN, TBN and TCN were next evaluated in DMSO/toluene mixture with different toluene fractions (f_T). As depicted in Fig. 1D and E, very weak fluorescence intensity was detected in pure DMSO of TCN. However, along with continuously enhancing the fraction of toluene to 99% in the mixtures, the emission intensity gradually increased, with a gradual redshift of the maximum emission to 680 nm, solidly demonstrating the AIE characteristics of TCN. Similarly, the AIE properties of TMN and TBN were also been confirmed in Supporting Information Fig. S20. The aggregates of TMN, TBN and TCN were intensely emissive and the emission intensities were boosted with 195, 105 and 29 times higher than that in pure DMSO solution, respectively. The three molecules (TMN, TBN, TCN) possess AIE properties because triphenylamine is commonly used as the scaffold structures for AIE molecule design, which is a classic donor structure with twisted three-dimensional spatial conformation. When these molecules are in the aggregated state, the molecular rotation is restricted, and the excited-state electrons can only return to the ground state through radiation-induced transition, thus enhancing the fluorescence. In addition, three AIEgens exhibited good photostability under white light irradiation (25 mW/cm^2) for 30 min (Supporting Information Fig. S21). Then the ROS production capacities of TMN, TBN and TCN were evaluated by different commercial fluorescent probes containing 9,10-anthracenediylbis (methylene)-dimalonic acid (ABDA, for $^1O_2$), hydroxyphenyl fluorescein (HPF, for ·OH) and dihydrorhodamine123 (DHR123, for $\cdot O_2^-$). As illustrated in Fig. 1F and G, when irradiating the mixture of ABDA and TCN with white light irradiation (25 mW/cm^2), the absorbance of ABDA at 378 nm decreased sharply and 79.0% of ABDA were consumed for 180 s. While the absorbance intensity almost no change in the ABDA alone group and the absorbance rapidly decreased by 24.0% in TMN, 30.9% in TBN, 9.6% in Ce6, and 19.5% in RB, respectively (Supporting Information Fig. S22), indicating that TCN displayed superior type II ROS production efficacy than other PSs. At the same time, TCN exhibited poor type I ROS (·OH and $\cdot O_2^-$) generation capacity (Supporting Information Figs. S23 and S24). To sum up, TCN is an excellent type II photosensitizer.

In order to obtain deeply insights into the optical characteristics of the AIEgens, density functional theory (DFT) calculations were conducted at the optimally tuned B3LYP/6-31G(d) level. In the optimized molecular conformations by DFT (Fig. 1H), the results revealed that the dihedral angle between methoxy-substituted triphenylamine (CTPA) unit and pyrene can result in more loose stacking and increase the contraction of AIEgens and oxygen, thereby improve the generation efficiency of ROS. Fig. 1I displayed that the electron clouds of the highest occupied molecular orbital (HOMO) are mainly delocalized throughout CTPA and pyrene unit suggesting good π-conjugation, while both thiophene and (2-(4-(pyridin-4-yl)phenyl)acetonitrile moieties dominating the lowest unoccupied molecular orbital (LUMO). The similar distributions of HOMO and LUMO were observed in TMN and TBN (Supporting Information Fig. S25). Besides, the calculation of single*t*-triplet energy gaps (ΔE_{ST}) demonstrated that the ΔE_{ST} of three molecules, including TMN, TBN and TCN, were 0.2331, 0.2247 and 0.1009 eV, respectively, all of which were relatively small and good for ROS generation (Fig. 1J). The above results implied that TCN exhibited the lowest ΔE_{ST}, which was beneficial for the production of ROS. In short, the theoretical calculation results were consistent with the ROS detection outcomes.

To enhance the delivery efficiency of TCN, EVs and M1-type MM were served as biomimetic hybrid carrier. Firstly, EVs derived from 4T1 cells and cell membranes derived from M1 phenotype macrophage were prepared, then EM@TCN were obtained by incubation-extrusion method. Subsequently, the aqueous hydrodynamic diameter of EVs, MM and EM@TCN were observed by dynamic light scattering (DLS), which were 102.7, 94.2 and 125.5 nm, respectively (Fig. 1K). The zeta potential values of EVs, MM and EM@TCN were -8.75 ± 0.29, -10.12 ± 0.78 and -11.14 ± 1.68 mV, respectively (Fig. 1L). These fascinated properties of EM@TCN supported them for further study *in vivo*, such as enhanced permeability and retention (EPR)[48]. Furthermore, there were no significant changes in the size of EM@TCN for following 7 days of storage in PBS and 10% FBS, suggesting that these particles were highly stable (Fig. 1M, Supporting Information Fig. S26). According to the standard curve of TCN (Supporting Information Fig. S27), drug loading efficiency of EM@TCN was $10.2 \pm 3.7\%$. Besides, the release profile of TCN from EM@TCN *in vitro* was studied. As shown in Supporting Information Fig. S28, upon white light irradiation, TCN was quickly released from EM@TCN, suggesting that ROS generated by TCN can disrupt the EM@TCN structure. As depicted in Fig. 1N, the transmission electron microscopy (TEM) images indicated the monodispersed EVs, MM and EM@TCN with uniform particle morphology, after illuminated with white

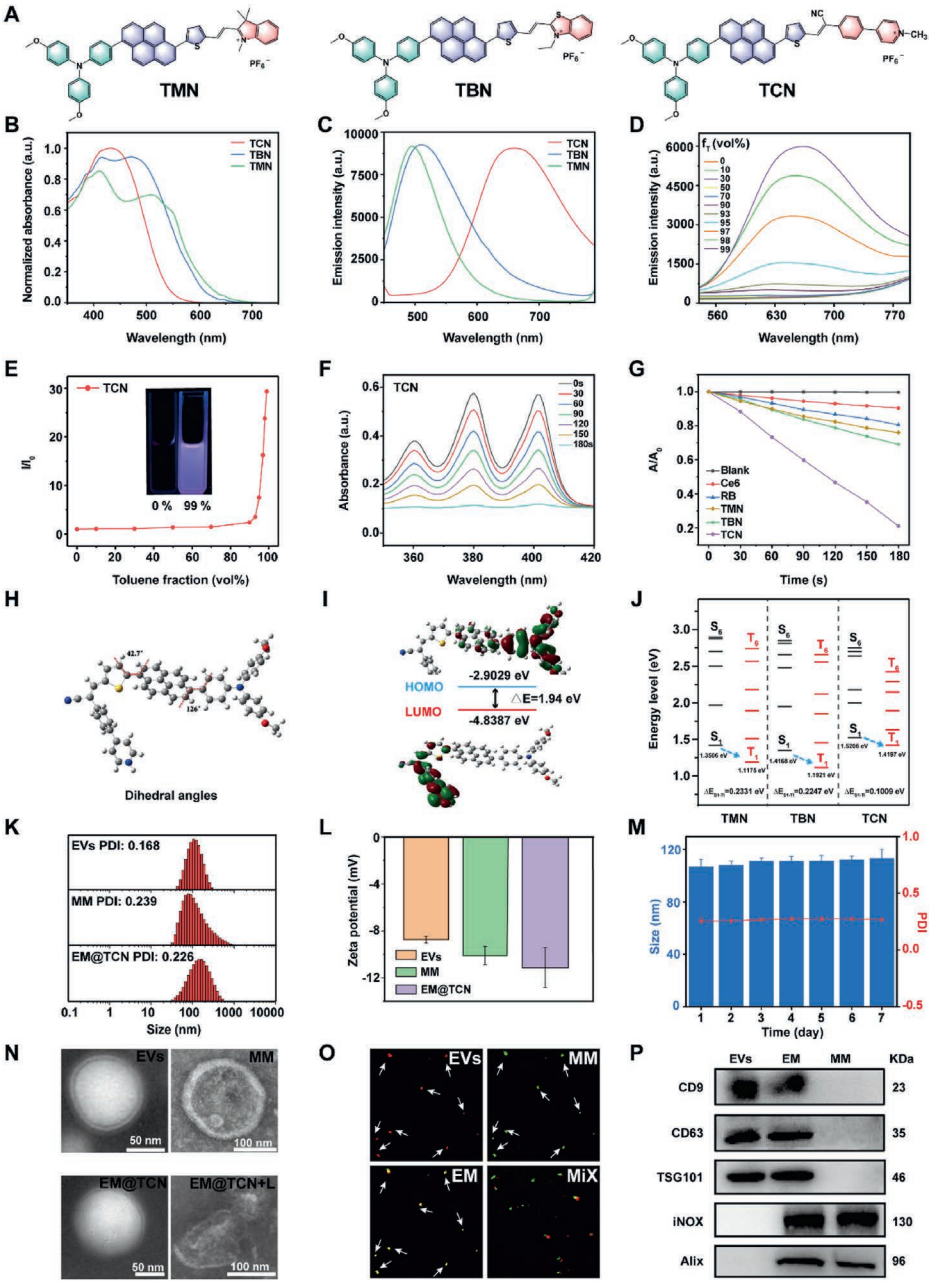

Figure 1 Preparation and characterization of EM@TCN. (A) Chemical structures of TMN, TBN and TCN. (B) Normalized UV-vis spectra of TMN, TBN and TCN (10 μmol/L) in DMSO solution. (C) Normalized emission spectra of TMN, TBN and TCN (10 μmol/L) in toluene solution (containing 1% DMSO, *v*/*v*). (D) Emission spectra of TCN in the mixed solution of DMSO/toluene with diverse ratios of toluene (f_T). (E) Plots of the relative emission intensity (I/I_0) versus toluene fraction of TCN. I_0 and I are the emission intensities of TCN in DMSO and DMSO/toluene mixtures, respectively. Inset: photos of TCN in DMSO ($f_T = 0$) and DMSO/toluene ($f_T = 99\%$) captured by 365 nm UV light. (F) UV-vis spectra of ABDA (50 μmol/L) used as a probe for the $^1O_2$ detection were incubated with TCN (10 μmol/L) under white light irradiation (25 mW/cm^2) at the predeterminate times. (G) Plots of the decline rates of ABDA with/without AIEgens and commercial photosensitizers (10 μmol/L) upon white light irradiation. A_0 and A represent the absorbance of ABDA before and after white light irradiation. (H) Dihedral angles based optimized ground state (S_0) geometries and (I) HOMO-LUMO distributions of TCN. (J) Energy levels of TMN, TBN and TCN. (K) Hydrodynamic size of EVs, MM and EM@TCN in aqueous solution. (L) Zeta potential values for EVs, MM and EM@TCN. (M) Hydrodynamic size and PDI of EM@TCN in PBS within 7 days ($n = 3$). The data are displayed as the mean ± standard deviation (SD). (N) TEM images of EVs, MM, EM@TCN and EM@TCN under white light irradiation for 15 min. (O) Confocal laser scanning microscope (CLSM) images of EVs, MM, EM or a simple mixture of EVs (Red) and MM (Green). (P) Exosomal markers including CD9, CD63, TSG101 and M1-type macrophage makers including iNOX and Alix were detected by Western blotting (WB).

light irradiation (25 mW/cm^2, 10 min), EM@TCN were disrupted, which was manifested as an increase of size. To confirm effective membrane fusion of EVs and MM in EM@TCN, EVs was stained with DiR and MM was labelled with DiO. The confocal images displayed good fluorescence colocalization (yellow) signals in the EM groups, as well as separated green and red signals in the simple mixture groups (Fig. 1O), confirming the fact that the nanovesicles had a high membrane fusion efficiency. Besides, Western blotting (WB) further confirmed that EM@TCN were phenotypically similar to EVs and M1 macrophage, showing simultaneous detection of exosome biomarkers CD9, CD63, and TSG101, as well as the expression of M1 macrophage-specific membrane proteins iNOX and Alix in the EM group (Fig. 1P). Additionally, the successful phenotypic change from M0 macrophages (RAW264.7 cells) to M1 macrophages was verified using an inverted microscope and flow cytometry (Supporting Information Fig. S29).

3.2. Subcellular organelle targeting and cytotoxicity study of AIEgens

The uptake efficiency of three AIEgens on 4T1 and HCT116 cells was investigated by CLSM at the varied time periods. We found that the uptake of AIEgens (red fluorescence signals) on 4T1 cells reached the highest level at 6 h and had a time-dependent variation (Fig. 2A). In addition, the similar tendency was also found on HCT116 cells, in which the red fluorescence intensity from AIEgens was increased along with the elevated incubation time (Supporting Information Fig. S30). To further evaluate their subcellular-organelle-targeting properties, the cellular imaging was performed on 4T1 and HCT116 cells *via* CLSM. As shown in Fig. 2B, after incubaqinghtions with TMN, TBN and TCN, respectively, reticulum-like mitochondria, round or oval-shaped lysosome and dotted or circular-shaped GA were obviously outlined, displaying strong fluorescence intensity and particularly

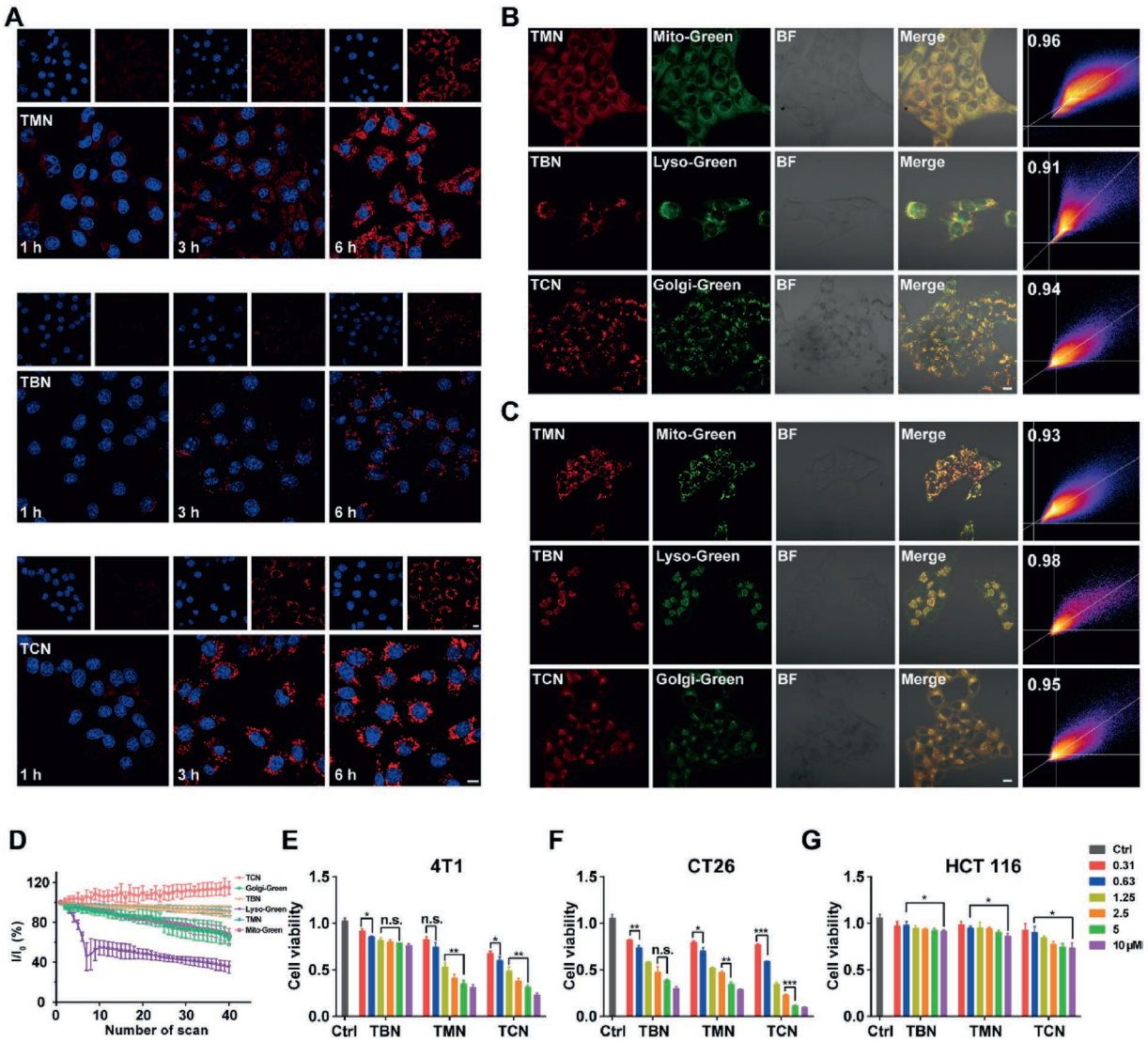

Figure 2 Cellular uptake, co-localization, photostability and cytotoxicity of AIEgens. (A) Cellular uptake study of AIEgens (10 μmol/L) on 4T1 cells. Scale bars: 10 μm. Co-localization analysis of AIEgens (10 μmol/L) and different commercial probes on (B) 4T1 cells and (C) HCT116 cells. Scale bar: 10 μm. (D) Loss of fluorescence in 4T1 cells stained with TMN, TBN, TCN, Mito-Green, Lyso-Green and Golgi-Green. Effect of treatment with various concentrations of AIEgens on the cytotoxicity of (E) 4T1 cells, (F) CT26 cells and (G) HCT116 cells. The data are displayed as mean ± SD and calculated by a Student's *t*-test. n.s.: no statistical significance, $^{*}P < 0.05$, $^{**}P < 0.01$, and $^{***}P < 0.001$.

high-contrast to background signal. To further assess their targeted selectivity, three fluorescent indicators including Mito-Green, Lyso-Green and Golgi-Green were applied to incubate with three AIEgens, respectively. For co-localization analysis, the Pearson's correlation coefficients (PCC) between the TMN and fluorescence image of Mito-Green were determined to be 0.96, the TBN and Lyso-Green image was 0.91, as well as the TCN and Golgi-Green image was 0.94 in 4T1 cells (Fig. 2B). The similar co-localization results were observed on HCT116 cells (Fig. 2C). As in Supporting Information Figs. S31−S33 depicted, these three AIEgens exhibited imperfect overlap with other commercial probes, demonstrating that three AIEgens possessed high targeting specificity, which further indicated that subtle structural modification can result in different targeting selectivity. Based on the above observations, it can be deduced that the mitochondria-targeting property of TMN may be ascribed to its highly efficient electrophoretic transmembrane transfer and the positive charge of the pyrrole moiety in TMN facilitates its binding to the negatively charged internal of the transmembrane potential of mitochondria[49]. Due to its high hydrophobicity, TBN inclines to form nano-sized aggregates in culture medium, and thus aggregates can be internalized into lysosome by cells endocytosis and specifically illuminate lysosomes once photoexcitation[50]. Cyanopyridinium salt moiety acts as the electron-acceptor group in TCN, which was proved to be an important functional group targeted Golgi apparatus[51]. In addition, photostability is as a critical index to estimate fluorescence imaging agents. Compared to commercial dyes concluding Mito-Green, Lyso-Green and Golgi-Green, there was minimal intensity loss detected in three AIEgens, demonstrating the high photobleaching resistance of TMN, TBN and TCN (Fig. 2D). Next, the cytotoxicity of AIEgens on 4T1, CT26 and HCT116 cells were evaluated using Sulforhodamine B (SRB) assay. As displayed in Fig. 2E−G, TCN plus white light irradiation (25 mW/cm^2, 10 min) showed the most apparent tumor-killing capacity in a concentration-dependent manner, whereas no significant dark toxicity was found in the AIEgens, except for TMN (Supporting Information Figs. S34 and S35). These results jointly demonstrated that TCN had excellent controllable phototoxicity and well biocompatibility in the dark among three AIEgens.

3.3. *Phototherapeutic effect of EM@TCN in vitro*

Firstly, the uptake of EM@TCN into 4T1 cells was analyzed by CLSM and FCM. As shown in Fig. 3A, EM@TCN can be absorbed into 4T1 cells, which illustrated by the increased red fluorescence signal and linear-scan spectrogram with prolonged costaining time. Subsequently, we performed the subcellular co-localization analysis of EM@TCN and Golgi-Green on 4T1 and HCT 116 cells by CLSM. As shown in Fig. 3B, when costaining with Golgi-Green, the red fluorescence signal of EM@TCN overlapped well with the green fluorescence signal of Golgi-Green. Above results demonstrated that EM@TCN can be effectively uptaken by cancer cells and exhibited excellent Golgi apparatus targeting capacity. The entrance pathways of the GA-targeting mechanism of EM@TCN in 4T1 cells were explored by employing various biochemical inhibitors. The fluorescence intensity of 4T1 cells that were incubated with EM@TCN at 4 °C or treated with the metabolic inhibitor 2-deoxy-D-glucose (2-DDG) was very weak (Supporting Information Fig. S36), implying an energy-dependent endocytosis process. To further determine the main mode of endocytosis induced by EM@TCN, specific inhibitors were utilized. The internalization of EM@TCN was only marginally affected by CHP, which inhibits clathrin-mediated endocytosis. In contrast, the treatments with MβCD (an inhibitor of lipid raft-mediated endocytosis) and GEN (an inhibitor of caveolae-mediated endocytosis) significantly reduced the uptake of EM@TCN by 45.1% and 65.1%, respectively. These outcomes suggest that EM@TCN mainly enters cells through an energy-dependent caveolae/raft-mediated endocytosis pathway. This is consistent with earlier studies that showed small molecules utilize similar endocytosis pathways to target GA[51]. According to Calcein-AM and PI live/dead costaining, the green fluorescence signal (live cells) of TCN or EM@TCN groups were resembled with the Control and Control + L groups. However, the EM@TCN plus white light irradiation (EM@TCN + L) group exhibited stronger red fluorescence signal (dead cells) than TCN plus white light irradiation (TCN + L) group (Fig. 3C and E). Besides, FCM analysis also displayed that the dead cell ratios treated with EM@TCN + L increased from 41.0% to 77.7% compared to TCN + L group (Supporting Information Fig. S37). These results indicated that the hybrid EVs and M1-type MM can promote the delivery of insoluble TCN further to improve the antitumor effect of the AIEgens. As shown in Fig. 3D and F, TCN + L induced an apoptosis rate of 67.0% on 4T1 cells, whereas, the apoptosis rate induced by EM@TCN + L group increased to 92.1%, which was significantly higher than the former. Besides, EM@TCN plus white light irradiation could increase the green fluorescence intensity of JC-M and decrease the red fluorescence intensity of JC-A, implying that it could reduce the mitochondrial membrane potential (MMP) and further lead to cell death (Fig. 3G). DCFH-DA was served as the total ROS fluorescence probe to determine the intracellular ROS production by different treatments. As demonstrated in Fig. 3H and J, EM@TCN + L group could generate robust ROS than TCN + L group, while negligible green fluorescence was detected in any other groups. The FCM quantitative analysis also showed a similar tendency with CLSM results (Fig. 3I). In addition, colony formation and scratch wound assay were utilized to evaluate the cell proliferation and migration capacity of 4T1 cells treated with various formulations. As demonstrated in Fig. 3K and N, the EM@TCN + L group could significantly inhibit the clonogenicity of 4T1 cells. What's more, the open wound area of EM@TCN + L was greater than other untreated groups, indicating that the biomimetic hybrid delivery system of EM@TCN plus white light irradiation possessed the strongest ability to inhibit 4T1 cells motility (Fig. 3L and O). The cell migration and invasion assays also exhibited consistent outcomes (Fig. 3M, P and Q). Nearly all the cells crossed the Transwell membranes with or without matrigel in the upper chamber at the Control, Control + L, TCN, and EM@TCN groups, but the number of invaded cells in TCN + L group was obviously decreased, especially in EM@TCN + L group. The migration rate and invasion rate of EM@TCN + L were 9.3% and 22.2%, respectively. The above results clearly demonstrated that EM@TCN could effectively uptaken by cancer cells and generate robust ROS upon white light irradiation to destroy MMP, inhibit cancer cells proliferation and migration, which eventually induce cell death.

3.4. *Pyroptosis and ICD elicited by EM@TCN in vitro*

Based on the previous researches, the production of enormous ROS instantaneously during PDT can induce serious inflammation response and arouse pyroptosis, which is an emerging and

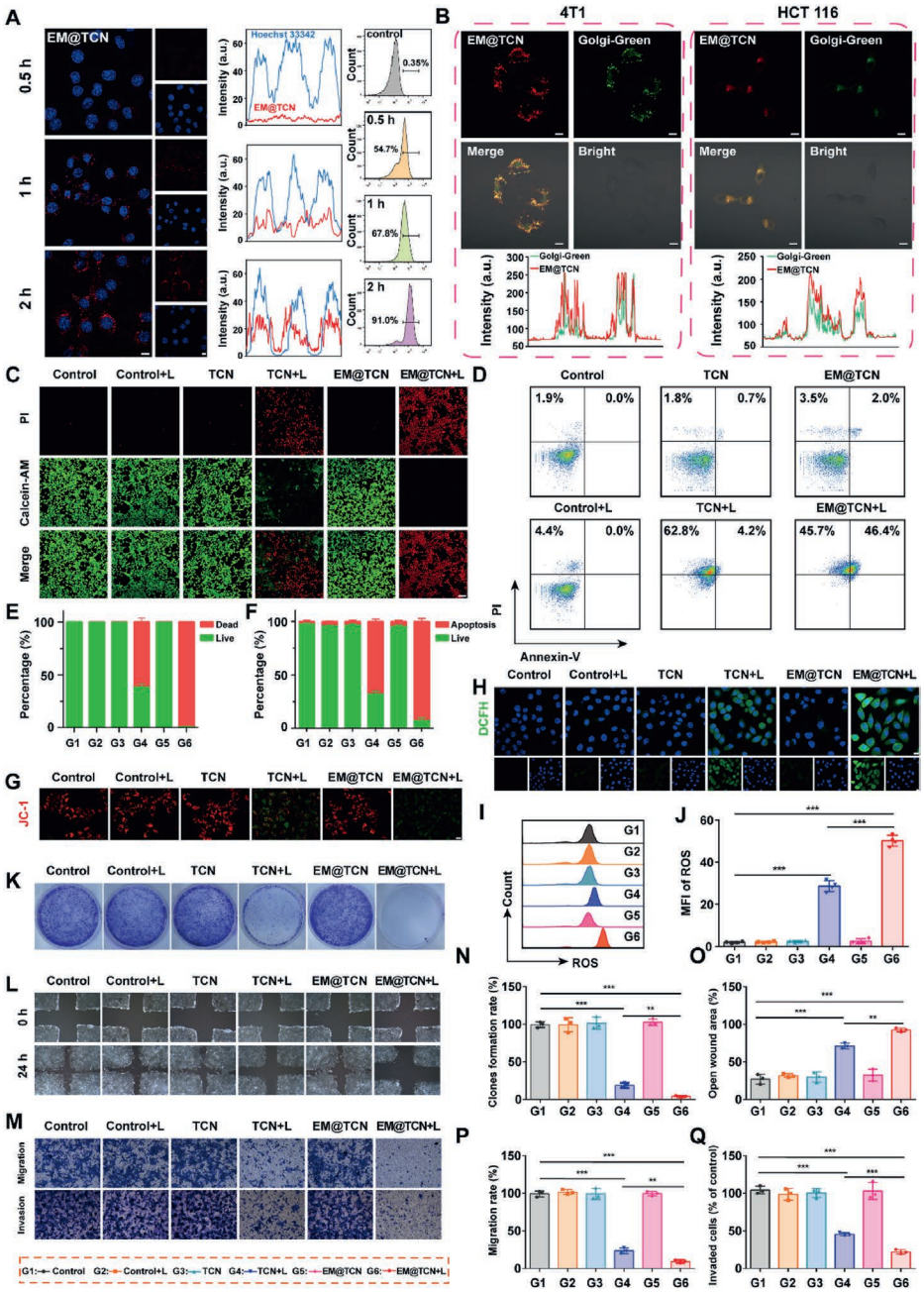

Figure 3 Phototherapeutic efficacy of EM@TCN *in vitro*. (A) Representative confocal images, its quantitative analysis and flow cytometry analysis of 4T1 cells treatment with EM@TCN at the scheduled times. Scale bars: 10 μm. (B) Subcellular colocalization CLSM images of EM@TCN and Golgi-Green in 4T1 and HCT116 cells. Scale bars: 10 μm. (C) CLSM images of live/dead costaining on 4T1 cells after various coincubation and (E) quantitative analysis. Scale bar: 100 μm. (D) Flow cytometry analysis of apoptosis on 4T1 cells and (F) quantitative analysis. (G) JC-1 assay of 4T1 cells after treated differently. Scale bar: 10 μm. (H) Intracellular ROS detection in 4T1 cells by CLSM and (J) quantitative analysis ($n = 4$). Scale bars: 10 μm. (I) Flow cytometry analysis of the total ROS in 4T1 cells after incubation with various preparations. (K) Representative photographs of colonies formation experiment and (N) quantitative analysis ($n = 3$). (L) Representative photographs of wound healing experiment and (O) quantitative analysis ($n = 3$). (M) Representative photographs of cell migration and invasion experiments and (P,Q) quantitative analysis ($n = 3$). The data are displayed as mean ± SD and calculated by a Student's *t*-test. $^{**}P < 0.01$, and $^{***}P < 0.001$.

regulated form of cell death typified by membrane integrity disruption, cell swelling and ballooning, and leak out various cytokines (Fig. 4A) [52-54]. Therefore, the morphological feature of 4T1 cells after treated with different preparations was firstly investigated by microscope to testify whether consistent with pyroptosis characteristics. As shown in Fig. 4B, the irradiation groups in TCN + L and EM@TCN + L were observed with blebbing-like and swelling pyroptotic cells (red arrows) after 20 min of PDT, in which the EM@TCN + L group could induce more serious cancer cell pyroptosis. CLSM imaging also exhibited the clear membrane bubbles in EM@TCN + L and TBN + L group (Fig. 4C). Besides, there was more significant and disrupted

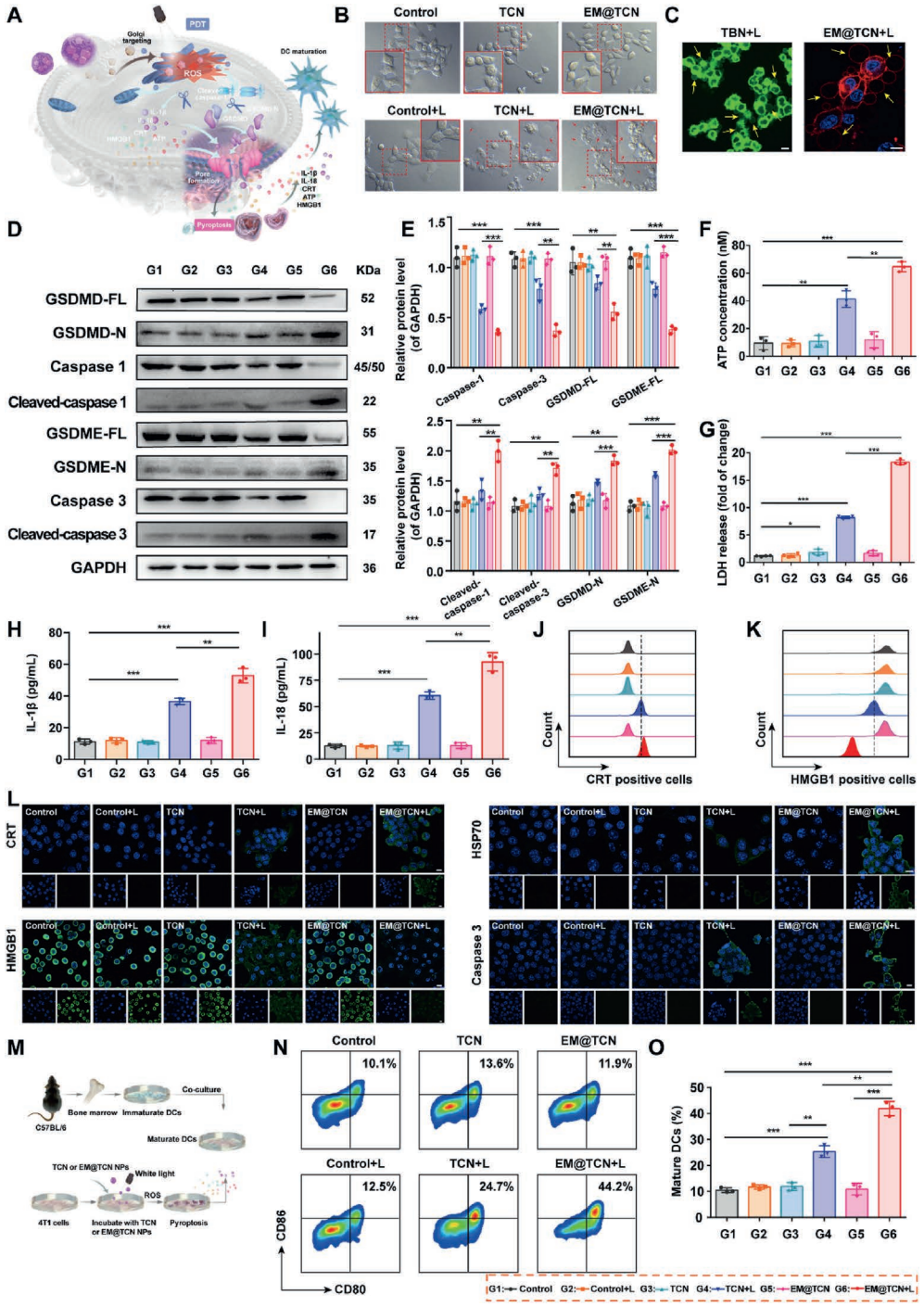

Figure 4 Photoinduced pyroptosis modulation of ICD immunosuppressive pathways. (A) Mechanism diagram of pyroptosis induced by EM@TCN plus white light irradiation to collectively lead to enhanced ICD. (B) Representative microscope photographs of 4T1 cells with different treatments. Red arrows displayed the pyroptotic cells. (C) Representative CLSM photographs of 4T1 cells treated with TBN or EM@TCN plus white light irradiation. Scale bars: 10 μm. (D) WB analysis of proteins expression associated with pyroptosis in 4T1 cells after treated with PBS, TCN and EM@TCN, in the presence or absence white light illumination (25 mW/cm^2) for 10 min. (E) Quantitative analysis in Fig. 4D ($n = 3$). (F) ATP release and (G) LDH release in 4T1 cell supernatant receiving diverse treatments ($n = 3$). (H) IL-1β secretion and (I) IL-18 secretion in 4T1 cell supernatant after subjected to various treatments ($n = 3$). Quantitative analysis of (J) CRT expression and (K) HMGB1 expression in 4T1 cells receiving various preparations by FCM ($n = 3$). (L) Immunofluorescence analysis of CRT, HMGB1, HSP70 and Caspase 3 in 4T1 cells treated differently. Scale bars: 10 μm. (M) Schematic diagram of BMDCs. (N) Representative FCM images of matured BMDCs ($CD11c^+CD80^+CD86^+$) *in vitro* ($n = 3$). (O) Quantitative analysis of matured BMDCs as shown in Fig. 4M ($n = 3$). The data are displayed as mean ± SD and calculated by a Student's *t*-test. $^*P < 0.05$, $^{**}P < 0.01$, and $^{***}P < 0.001$.

bubbles generation along with the extended irradiation time (Supporting Information Fig. S38). Above experiments have demonstrated that TCN is an AIE photosensitizer specially targeting Golgi apparatus, which can generate high levels of ROS *in situ*. GM130 protein is an important component of Golgi matrix, the changes of its expression level can disrupt the structure of Golgi apparatus, leading to a loss of cell polarity and an increase in tumor migration and invasion characteristics[55,56]. With this in mind, the expression of GM130 was firstly investigated using WB. As Supporting Information Fig. S39 demonstrated, the expression of GM130 on 4T1 cells was downregulated after treatment with TCN + L or EM@TCN + L, and the latter had more pronounced effect, suggesting that EM@TCN + L could significantly disrupt the structural integrity of GA and activate the related signal pathways. Pyroptosis plays an extremely important role in various physiological and pathology progresses that are executed by caspase-mediated gasdermin D (GSDMD) and gasdermin E (GSDME)[57]. In this progress, the GSDM family were cleaved by Caspase 1/4/11/5 or Caspase 3, then released GSDMD-N and GSDME-N fragments, respectively, which induced the production of cell pyroptosis, further promoting responsible for membrane perforation and triggering the activation of host immune system[58-61]. Consequently, according to the observed phenomenon mentioned above, the expression of pyroptosis-related proteins was tested by WB. As depicted in Fig. 4D, E and Supporting Information Fig. S40, EM@TCN + L group lead to the highest expressions of GSDMD-N and cleaved Caspase 1. At the same time, the irradiation group of EM@TCN + L also could significantly cause the GSDME-N and cleaved Caspase 3 overexpression. Collectively, these results suggested that GA-targeted EM@TCN generates a significant amount of ROS *in situ* under white light irradiation, which directly resulted to membrane damage and subsequently induced photon-controlled pyroptosis. In addition, during the process of pyroptosis, the pores formed on plasma membrane could release the extracellular contents including adenosine triphosphate (ATP), lactate dehydrogenase (LDH), and inflammatory cytokines such as interleukin-1 beta (IL-1β) and interleukin-18 (IL-18), to the outside of the cell[62]. As shown in Fig. 4F, the ATP released in 4T1 cells supernatant was dramatically higher after EM@TCN plus white irradiation treatment. Similarly, EM@TCN + L group had the maximal level of LDH release (Fig. 4G). Furthermore, as depicted in Fig. 4H and I, the levels of IL-1β and IL-18 in 4T1 cell supernatant treated with EM@TCN plus white light irradiation exhibited the highest release compared to the other groups. Collectively, these results solidly demonstrated that the pyroptosis pathway was successfully activated by EM@TCN + L during PDT process. It is widely accepted that the abundant ROS generation induced pyroptosis were a typical type of ICD. We next study the major hallmarks of ICD sequentially. Calreticulin (CRT) serves as an "eat me" signal, elicitation of high-mobility group protein B1 (HMGB1) nuclear release and release HSP70 are three typical features of ICD in tumor cells[63]. The FCM analysis showed that EM@TCN could significantly promoted the translocation of CRT and the release of HMGB1 from the nucleus under white light irradiation (Fig. 4J and K). The similar results were also observed by CLSM (Fig. 4L, Supporting Information Fig. S41). Moreover, in comparation with the TCN + L group, the EM@TCN + L group also boosted the levels of HSP70 release. Besides, numerous ROS production in PDT could effectively induce DNA damage. When 4T1 cells were incubated with EM@TCN under white light irradiation showed bright green fluorescence of γ-H_2AX than other treatment groups, with an enhanced γ-H_2AX positive area of ~9.5- and ~2.0-fold compared to Control and TCN + L group, respectively (Supporting Information Fig. S42). Taken together, these outcomes obviously demonstrated that biometric hybrid EVs and M1-type MM coated EM@TCN can effectively induce tumor cells pyroptosis through photoinduced PDT. In order to further investigate that the cancer cells undergoing photoinduced pyroptosis can more effectively promote systematic immune responses, 4T1 cells after subjected with various treatments were cultivated with bone marrow-derived dendritic cells (BMDCs) *in vitro*, the dendritic cells (DCs) maturation ($CD11c^+CD80^+CD86^+$ cells) of each group were measured by FCM (Fig. 4M). As depicted in Fig. 4N and O, the ratios of $CD11c^+CD80^+CD86^+$ DCs in EM@TCN + L group was 44.2%, which were 3.5 and 1.8 folds compared with Control + L (12.5%) and TCN + L group (24.7%), respectively, displaying that EM@TCN + L undergoing pyroptosis process could elicit the most robust immunogenicity, thus resulting in a more efficient tumor antigen presentation. Additionally, M1-derived extracellular vesicles (EVs) have been reported to inherit certain functions from their parental M1 macrophages, including the modulation of the tumor microenvironment (TME) by converting M2 macrophages into the M1 phenotype[64]. Therefore, we aimed to determine whether the biometric hybrid nanosystem EM@TCN could induce macrophage repolarization under white light irradiation. As shown in Supporting Information Fig. S43, treatment with pure M1-type macrophage membranes (M1-type MM) led to a decrease in $F4/80^+CD206^+$ M2 macrophages and an increase in $F4/80^+CD86^+$ M1 macrophages to some extent. Upon exposure to light irradiation, the EM@TCN + L group showed a significant repolarization of M2 macrophages towards an antitumor M1 phenotype. This effect can be attributed to the combined action of M1-MM and the AIE photosensitizer TCN plus white light irradiation, which jointly re-educate macrophages. In short, the above results indicated that photoinduced pyroptosis and ICD by EM@TCN plus white light irradiation can not only boost inflammatory molecule expression, but also activate the release of DMAPs, further to effectively elicit the immune response.

3.5. RNA-seq analysis on the therapeutic mechanism of EM@TCN

To further elucidate the underlying mechanism of EM@TCN plus white light irradiation in cellular transcriptome modulation, we investigated the RNA sequencing analysis on 4T1 cells subjected to different treatments. Firstly, the gene distribution differences between diverse groups were characterized by volcanic plots. As shown in Fig. 5A, there were few significant differences in gene distribution between the Control group and EM@TCN groups, whereas, between the Control and EM@TCN + L, EM@TCN and EM@TCN + L groups, there were much differentially expressed genes (DEGs). Next, in order to unveil the changes in the mRNA biological function and its impact on related pathways, we executed gene ontology (GO) and Kyoto Encyclopedia of Genes and Genomes (KEGG) enrichment analyses. As depicted in Fig. 5B and C, the main differences in the EM@TCN + L treated 4T1 cells prior to and post PDT was involved in protein activation cascade, acute inflammatory response, regulation of apoptotic cell clearance and regulation of humoral immune response, etc. As Fig. 5D displayed, KEGG pathway analyses suggested that the DEGs of 4T1 cells treated with EM@TCN with white light

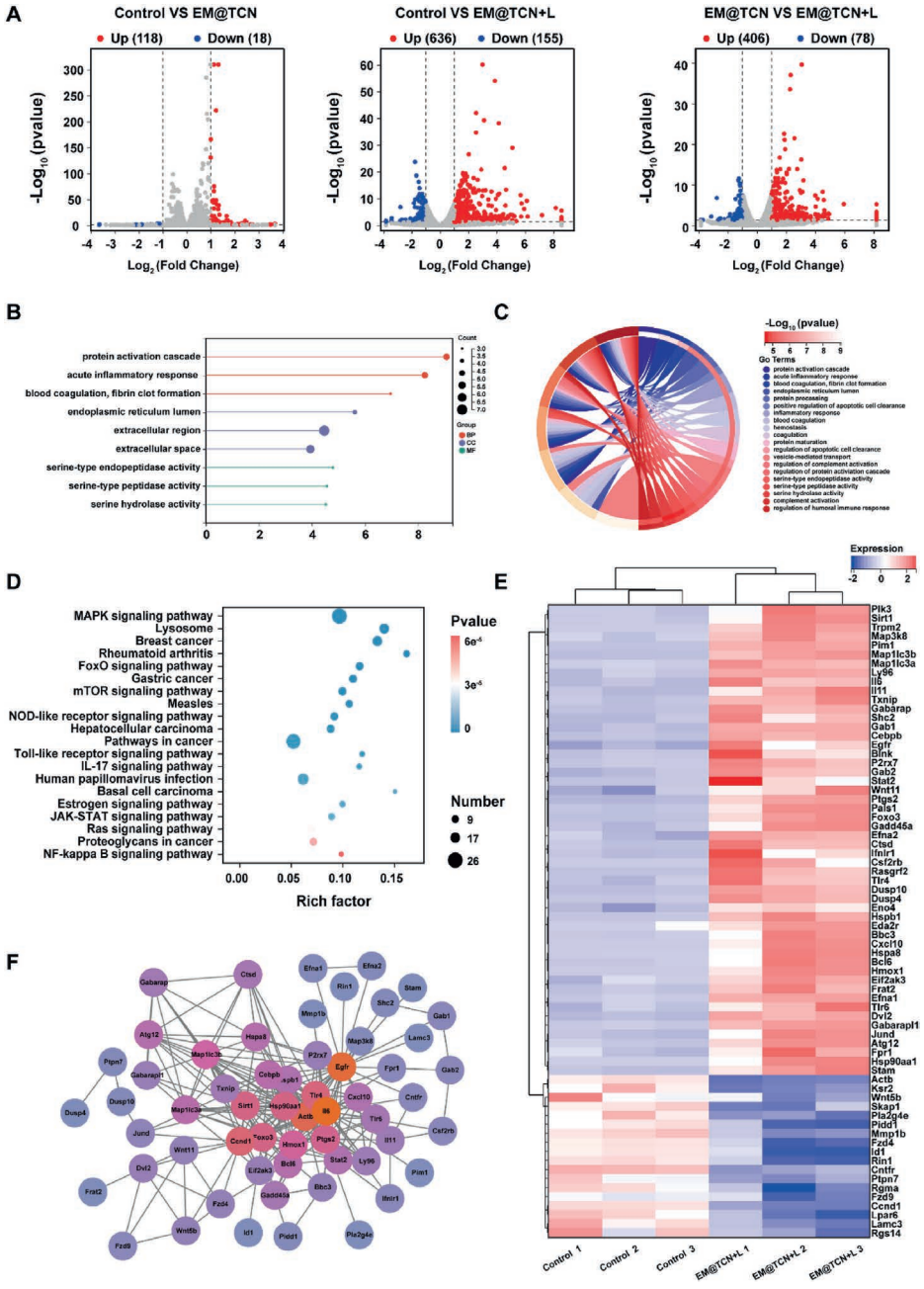

Figure 5 RNA sequencing analysis of 4T1 cells receiving various treatments. (A) The volcano plots of differentially expressed genes (DEGs) in each group. (B, C) Gene ontology (GO) analyses of the DEGs and the enriched chord plots of the Go enrichment analysis between the EM@TCN + L group and Control group (BP, biological process; CC, cellular components; MF, molecular function). (D) Kyoto Encyclopedia of Genes and Genomes (KEGG) pathway distributions of DEGs. (E) Heat map of DEGs at various treatments. (F) Protein−protein interaction network of functional intersecting genes.

irradiation were enriched in inflammatory signaling pathways, such as MAPK, NOD-like receptor, IL-17 and NF-κB signaling pathways, which demonstrated that the EM@TCN plus white light irradiation treatment can efficiently kill cancer cells and elicit inflammation, which may be attributed to photoinduced pyroptosis. We also plotted DEGs heat map and protein-protein interaction network related to pyroptosis to further explore their potential mechanisms (Fig. 5E and F). We analyzed the expression levels of DEGs and found that 52 upregulated and 18 downregulated genes were identified in Control group compared to EM@TCN + L group (Fig. 5E, the first 70 lines). Most upregulated genes were associated with programmed cell death. Then, the protein-protein interactions network was mainly involved in programmed cell death associated functional pathway, such as IL-17 and NF-κB signaling pathways (Fig. 5F). These results confirmed that EM@TCN plus white light irradiation can effectively provoke pyroptosis to enhance tumor immunogenicity and generate a strong antitumor immune response.

3.6. Biodistribution and antitumor effect on subcutaneous 4T1 tumor model

Based on the superior performance through effectively inducing pyroptosis and ICD to promote the DCs maturation of EM@TCN *in vitro*, we next evaluated its antitumor performance *in vivo* animal experiments using BALB/c mice. In order to achieve TCN intravenously administration *via* tail vein, we prepared TCN dots as a reference administration mode *in vivo* delivery. Firstly, the biodistribution and tumor accumulation capability of prepared TCN dots and EM@TCN were investigated. 4T1-bearing-tumor mice were intravenously administrated with TCN dots or EM@TCN *via* tail vein and imaged by IVIS imaging system at the scheduled times. The results showed that mice injected with EM@TCN exhibited stronger fluorescence intensity than TCN dots treatment group, and their fluorescence intensity peaked at about 12 h post-injection and then declined (Fig. 6A). Notably, a strong fluorescence intensity was occurred in the EM@TCN group even at 32 h after injection, whereas there was a weak fluorescence in the TCN dots group, indicating the specific enrichment and long retention of EM@TCN at the tumor site (Fig. 6B). After 32 h injection, the mice were executed and the main organs did not exhibit obviously fluorescent signal, nevertheless, there was an apparently fluorescent signal in tumors of the EM@TCN group (Fig. 6C), further demonstrating its excellent tumor-specific accumulation ability, extending circulation and detention time. Subsequently, a 4T1-bearing-tumor mouse model using BALB/c mice was established to determine the anticancer performance of EM@TCN *in vivo*. According to the dosing regimen, as depicted in Fig. 6D, when the tumor volume attained approximate 100 mm^3, the mice were irregularly assigned into 6 groups ($n = 6$): 1) Control, 2) Control + L, 3) TCN dots, 4) TCN dots plus white light irradiation (TCN dots + L), 5) EM@TCN, 6) EM@TCN plus white light irradiation (EM@TCN + L). PBS, TCN dots or EM@TCN were intravenously injected into the mice at an equal TCN dose of 4 mg/kg. The tumor region of irradiation groups was illuminated with white light irradiation (150 mW/cm^2, 8 min) after 12 h post-injection. The alteration of tumor volume and body weight were recorded throughout the entire treatment period. As illustrated in Fig. 6E, F and H, the single employment of AIEgens or white light irradiation alone could not inhibit tumor growth, whereas the mice treated with EM@TCN plus white light irradiation exhibited more effective tumor inhibition compared with the TCN dots + L group, which fully indicated the biometric hybrid nanoparticles could effectively delivery TCN into the tumor of mice and promote PDT induced synergistic pyroptosis and ICD treatment. Moreover, there were no noticeable weight loss of the mice during the treatment period (Fig. 6G). The temperature change of the tumor site in mice was measured in the anti-tumor experiment *in vivo* when the tumor was irradiated by white light (150 mW/cm^2, 8 min), showing an increase of about 5 °C (Supporting Information Fig. S44). To evaluate the hepatotoxicity and nephrotoxicity in diverse treatment groups, we detected the biochemical indexes of serum, which revealed that all main parameter values remained a standard level, demonstrating that EM@TCN had excellent biosafety (Supporting Information Fig. S45). Taken together, these results verified the potent antitumor efficacy and negligible systemic toxicity of EM@TCN with white light irradiation *in vivo*.

Inspired by EM@TCN plus white light irradiation showing excellent pyroptosis accompanied by ICD concurrently *in vitro*, we further studied the immune response performances *in vivo* of photoinduced EM@TCN + L by FCM. It is widely known that PDT photoinduced by pyroptosis and ICD effectively promoted the maturation of DCs, which are the most powerful antigen presentation cells (APCs). To further activate in response to tumor-associated antigens (TAA) and stimulate the systemic antitumor T cell immune response[65]. DCs in spleens and tumors were firstly analyzed. As displayed in Fig. 6I and Supporting Information Fig. S46C, TCN dots or EM@TCN plus white light irradiation could increase the $CD11c^+MHCII^+$DCs cell counts in tumors, and the latter was more significant, which was 18.9% and 26.5%, respectively. The similar results were observed in the spleens (Fig. S46A and S46B). Another index of matured $CD80^+CD86^+$ DCs was also evaluated, and the ratios of $CD80^+CD86^+$ DCs was poor in Control or white light irradiation alone treatment groups in spleens, but the DCs maturation ratios of EM@TCN + L group reached 20.7%, showing nearly 2.1 folds greater efficacy than that in the TCN dots + L group (9.9%) (Fig. 6M). Mature DCs plays a crucial role in antigen presentation to T cells, thereby boosting infiltration of cytotoxic T cells in the tumors. As we can see, the infiltration ratio of $CD3^+CD8^+$ T cells in EM@TCN + L group reached 18.7%, which were 1.6 folds higher than TCN dots + L group (11.9%) in spleens (Fig. 6J and N). At the same time, after treated with EM@TCN + L, the rates of $CD3^+CD8^+$ T cells obviously increased to 32.5% from 10.8% in Control group in the tumors (Fig. 6O). Activated tumor associated macrophages (TAMs) mainly conclude M1-like macrophages and M2-like macrophages. M2-like TAMs, as a protumoral macrophage, can promote tumor development and immune scape through release of inflammatory factors. M1-like TAMs, as an antitumoral macrophages, can facilitate antitumor immune response and further lead to cancer cell death[66]. To evaluate the influence of EM@TCN + L on M1-like and M2-like macrophage in the spleens, these two phenotype ratios were analyzed by FCM. As Fig. 6P and Q shows, the percentages of $F4/80^+CD86^+CD206^-$ M1-like macrophage and $F4/80^+CD86^-CD206^+$ M2-like macrophage treated with EM@TCN + L was 21.0% and 5.3%, respectively, which there was a 11.7% increase in M1 phenotype macrophages and a 22.7% decline in M2 phenotype macrophages in comparation with Control group in spleens. Regulatory T cells (Tregs) as main immune suppressive cells, which can inhibit the activation of antitumor immune response and promote tumor development[67]. To investigate the influence of EM@TCN + L on this cell, excised tumors were analyzed by FCM. As Fig. 6R depicted, the ratios of $CD4^+CD25^+$ Tregs in EM@TCN + L group (2.5%) downregulated compared with TCN dots + L group (6.8%) and Control group (12.7%) in the tumors. Similarly, myeloid derived suppressor cells (MDSCs), as precursors of DCs, macrophages and granulocytes, are playing an important role in immune suppression through impairing T cell activity and facilitating the growth and metastasis of tumor[68,69]. As depicted in Fig. 6K and S, the percentages of $CD11b^+Gr\text{-}1^+$ MDSCs of Control group (78.6%) were significantly inhibited by the TCN dots + L (69.3%) and EM@TCN + L treatments (48.2%), especially in EM@TCN + L group in spleens. These results demonstrated that EM@TCN plus white light irradiation could inhibit Tregs aggregation, further suppress tumor immune escape and facilitate more efficient antitumor effects.

Besides, the main organs and tumor slices were also detected by hematoxylin and eosin (H&E), Ki67 and dUTP nick end labeling (TUNEL) staining, which implied that there were no pathological changes of main organs, and EM@TCN plus white light could significantly inhibit tumor proliferation and promote

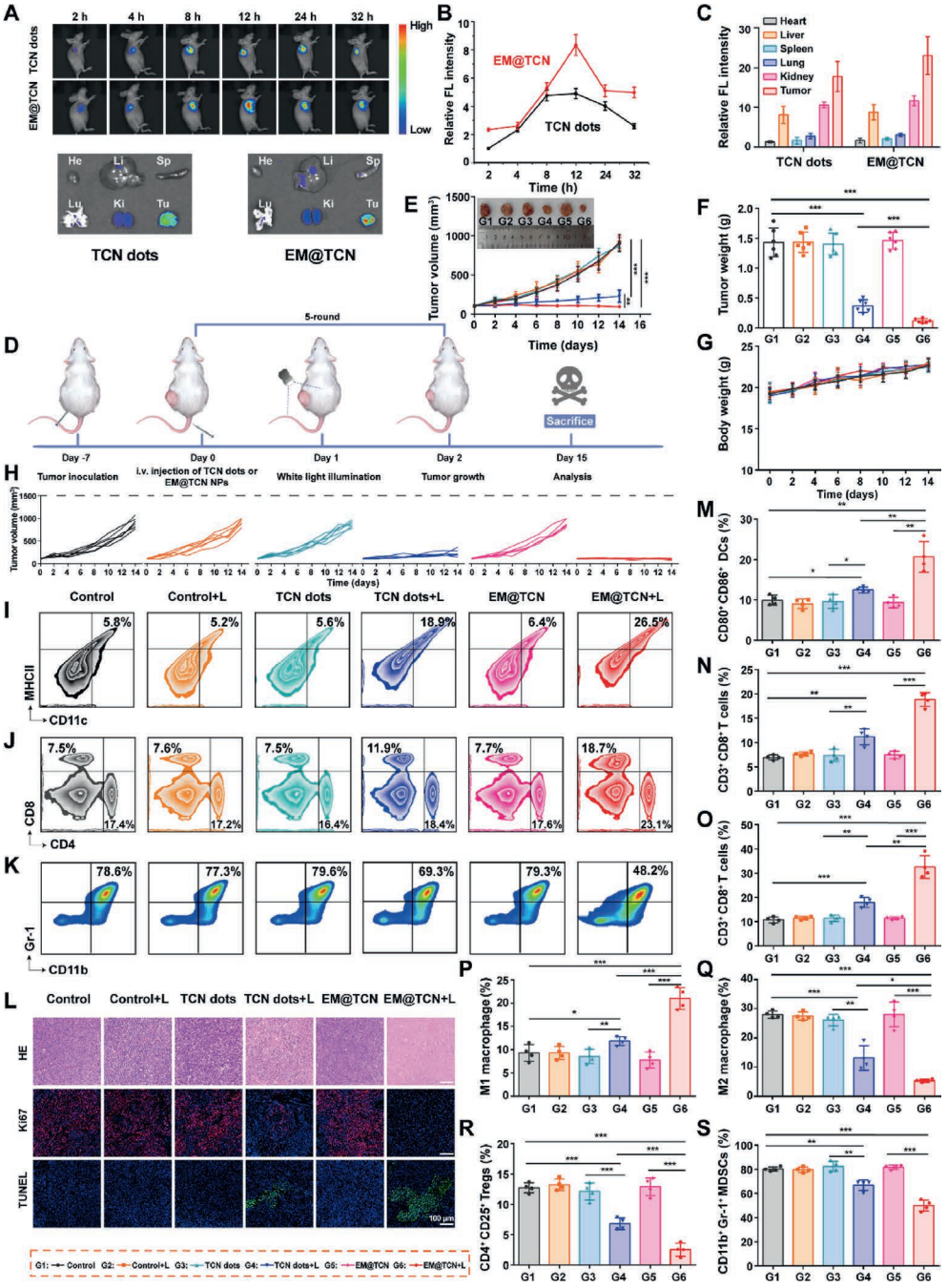

Figure 6 Distribution and antitumor efficacy of EM@TCN on subcutaneous 4T1-bearing-tumor mouse model. (A) Representative fluorescent photographs of mice treated with TCN dots or EM@TCN at the scheduled times and fluorescent photographs of main organs and tumors after intravenously with TCN dots or EM@TCN for 32 h. (B) Quantitative analysis fluorescence intensity of tumor regions at the scheduled times. (C) Relative fluorescence intensity of main organs and tumors at 32 h post-injection ($n = 3$). (D) Schematic diagram of the therapeutic strategy in 4T1 subcutaneous tumor model. (E−G) Changes of tumor growth curves, tumor weight and body weight values after administrating the different indicated treatments. Inset: representative photographs of dissected tumors after 15 days treatments ($n = 6$). (H) Individual tumor growth curves in each group ($n = 6$). Representative FCM images of (I) $CD11c^{+}MHCII^{+}$ DCs in tumors, (J) $CD8^{+}$ T cells in spleens and (K) $CD11b^{+}Gr\text{-}1^{+}$ MDSCs in spleens ($n = 4$). (L) H&E, Ki67 and TUNEL staining of tumor slices in each group ($n = 6$). Scale bar: 100 μm. (M-S) Relative percentage of diverse immune cells treated differently. The data are displayed as mean ± SD and calculated by a Student's *t*-test. $^{*}P < 0.05$, $^{**}P < 0.01$, and $^{***}P < 0.001$.

cancer cells death (Fig. 6L, Supporting Information Fig. S47). These results jointly proved that EM@TCN plus white light irradiation can significantly suppress the growth of tumor through photoinduced pyroptosis. Subsequently, the DCs maturation remodeled immunosuppressive microenvironment and potentiated CTLs infiltration, TAMs repolarization and decreased infiltration of immune suppressive cells (MDSCs and Tregs), leading to a robust adaptive immunity response for photoimmunotherapy.

3.7. Abscopal effect on 4T1 bilateral tumor model

Subsequently, we constructed a bilateral 4T1-bearing-tumor mouse model and investigated whether EM@TCN plus white light irradiation could induce systemic immune response and suppress the development of distant tumor. As Fig. 7A showed, when the primary tumor attained approximate 100 mm^3, the mice were irregularly assigned into 6 groups, including 1) Control, 2) Control + L, 3) TCN dots, 4) TCN dots + L, 5) EM@TCN, 6) EM@TCN + L groups. The primary tumor was intravenously injected the corresponding formulations *via* tail vein every 3 days, after injection for 12 h and the illumination groups was subjected to white light (150 mW/cm^2, 8 min), while the distant tumor was untreated and kept growing naturally. The mice weight, primary and distant tumor volume were monitored every other day. On the 15th day, the tumors and spleens of mice were dissected to analyze by FCM and immunofluorescence staining. As shown in Fig. 7B, no statistically significant weight loss of the mice was found between the different treatments throughout the entire treatment period. The growth of bilateral tumors treated with TCN dots + L were obviously inhibited, while EM@TCN + L had a more significant inhibition on bilateral tumors (Fig. 7C−E). The primary and distant tumor weight of mice in the EM@TCN + L group were 0.1 and 0.2 g, respectively, which significantly reduced compared with Control group (Fig. 7F). Therefore, we can draw a conclusion that with hybrid EVs and M1-type MM coated, EM@TCN plus white light irradiation can effectively inhibit the distant tumor growth through systematic immunity *via* pyroptosis[70].

To further study the immunological mechanism of pyroptosis-mediated photoimmunotherapy elicited by EM@TCN + L, the distant tumor was analyzed by FCM on the end of treatment. On the basis of that DCs can stimulate and connect innate and adaptive immune response, we firstly analyzed the DCs maturation in the spleens. As depicted in Supporting Information Fig. S48, EM@TCN + L treatment (60.0%) could significantly facilitate the maturation of $CD80^+CD86^+$ DCs in comparation with the Control group (12.8%) in the spleens. To further investigate the immune response provoked by DCs, tumor-infiltrating cytotoxic T lymphocyte cells were determined in tumors and spleens. As shown in Fig. 7G and L, in comparation with TCN dots + L group, the EM@TCN + L treated group had a more powerful capacity of activating of effector T cells in spleens. It is worthy of note that the ratios of $CD3^+CD4^+$ T cells was 31.7%, which was 1.8 folds higher than TCN dots + L group (17.7%). Similarly, the populations of $CD3^+CD8^+$ T cells in EM@TCN + L group has increased from 6.4% to 9.5% compared with TCN dots + L group in spleens, suggesting that the specific systematic immune response was activated by pyroptosis induced photoimmunotherapy (Fig. 7H and M). All of these results exhibited the similar trend on the tumors (Fig. 7N, Fig. Supporting Information Fig. S49A). When TAMs repolarize from M2-like phenotype to M1-like phenotype, the immunosuppressive TME is reversed, further to promote antitumor immunity[71]. As illustrated in Fig. 7I and O, EM@TCN plus white light irradiation (54.7%) obviously enhanced the ratios of $F4/80^+CD86^+CD206^-$ M1-like macrophage in tumors, which was 5.6 and 2.1 folds higher than Control (9.7%) and TCN dots + L group (26.0%), respectively. And the proportions of $F4/80^+CD86^-CD206^+$ M2-like macrophage in EM@TCN + L group (14.8%) remarkably reduced to the lowest level in comparation with the Control group (29.0%) in tumors (Fig. 7J and P). The similar results were obtained in spleens (Fig. S49B and S49C). These outcomes indicated that EM@TCN plus white light irradiation could reverse immunosuppressive TME and promote antitumor effects. An immunologic memory effect generation is result of adaptive immune response[72]. Therefore, $CD4^+$ and $CD8^+$ T cells in the tumors were separated to determine the ratios of central memory T cells (T_{CM}) and effector T cells (T_{EM}), respectively. Obviously, the mice in the EM@TCN + L group exhibited much greater $CD4^+CD44^+CD62L^+$ T_{CM} or $CD8^+CD44^+CD62L^+$ T_{CM} than the other groups in distant tumors, demonstrating that EM@TCN + L could produce a long-term immunological response (Fig. 7R and Fig. S49D). Besides, the ratios of $CD4^+CD25^+$ Tregs in EM@TCN + L group decreased from 17.8% to 3.0% in comparation with Control group in the spleens (Fig. 7Q). Similarly, the EM@TCN + L group (3.4%) apparently decreased the proportions of $CD4^+CD25^+$ Tregs in comparation with Control (20.3%) and TCN + L group (10.0%) in the tumors (Fig. S49E). To further confirm the systematic immune response of various treatments, the tumor slices of all groups were evaluated by immunofluorescence staining. As displayed in Fig. 7K, the bright red fluorescence signal for CRT and almost no red fluorescence signal for HMGB1 was found in the tumors of EM@TCN + L group. In addition, immunofluorescence images further confirmed in the EM@TCN + L group exhibited the most pronounced cleaved Caspase 1 and GSDMD-N expression upregulation. Collectively, above results confirmed that pyroptosis coactivated by EM@TCN plus white light irradiation can trigger intense immune response, attributing to the enhanced tumor immunogenicity and reshaped immune TME.

3.8. Combination antitumor effect of EM@TCN + L and αPD-L1 on 4T1 subcutaneous tumor model

The remodeling of TME after EM@TCN plus white light irradiation treatment concluded boosting T cells infiltration and declining immunosuppressive cells, created a crucial condition for enhancing the sensitivity to ICB therapy. Based on this, the synergism ability of EM@TCN + L combined with αPD-L1 to elicit systemic immunity were further explored. Firstly, we constructed a 4T1-bearing-tumor model to study the tumor suppression effect of mice treated with PBS (Control), αPD-L1, EM@TCN + L and EM@TCN + L + αPD-L1, respectively. During the period of 15 days, the tumor size and mouse mass were continuously recorded every 2 days. As depicted in Fig. 8A, the corresponding formulations were intravenously to the mice through tail vein, expect for αPD-L1 was intraperitoneal injection (EM@TCN at an equal TCN dose of 4 mg/kg, αPD-L1: 10 mg/kg). As shown in Fig. 8B and C, the αPD-L1 group exhibited a poor therapeutic efficacy while the EM@TCN + L group exhibited an apparent tumor growth inhibition, and this suppression can be more significant once it was combined with αPD-L1. During the observation periods, the mice weight with diverse treatments were upon acceptable fluctuations, displaying good biosafety of the

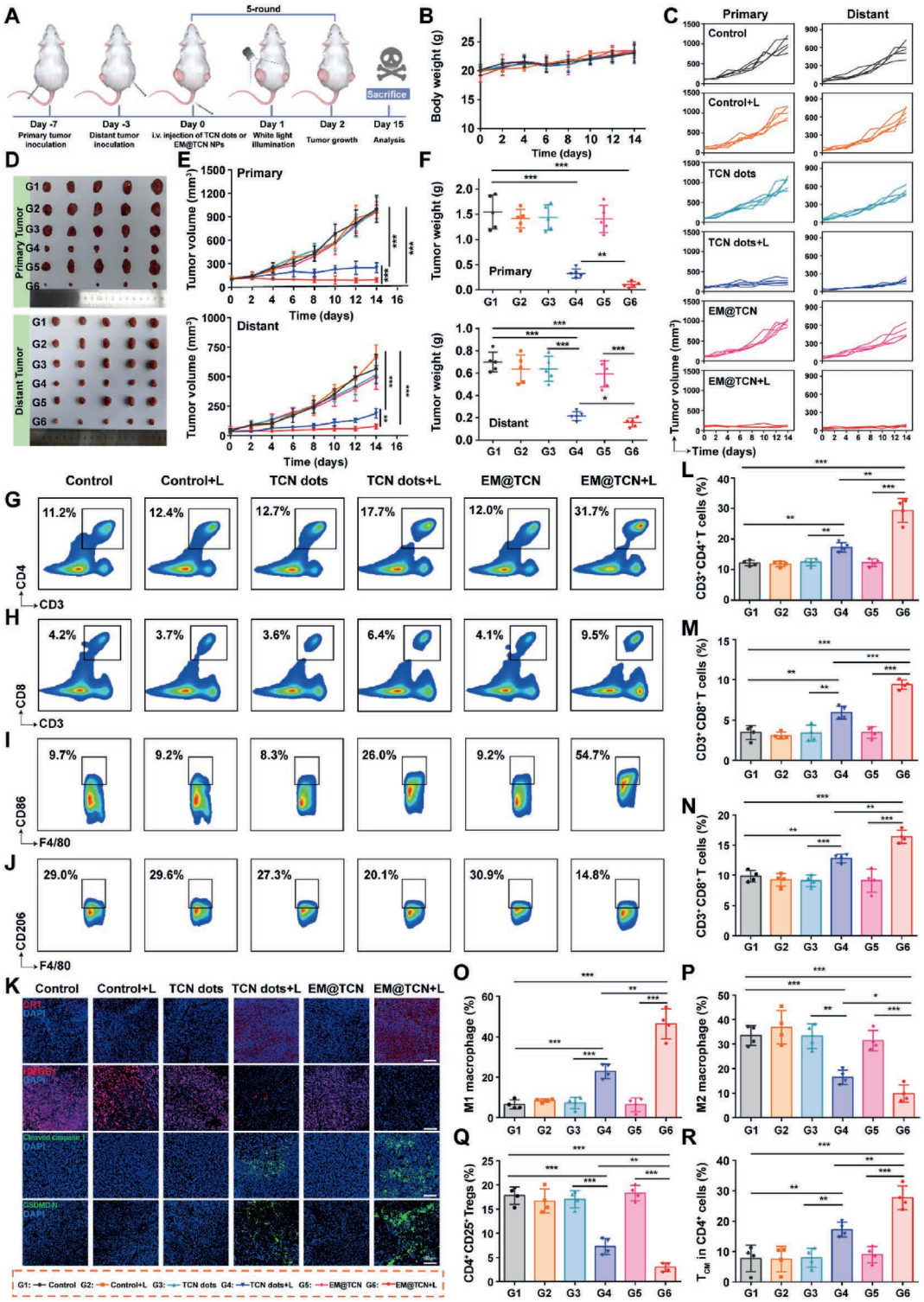

Figure 7 Anticancer effect based on 4T1 bilateral tumor model. (A) Schematic diagram of the therapeutic strategy in 4T1 bilateral tumor model. (B) Changes in body weight among each group. (C) Individual growth curves of bilateral tumors of mice with various preparations. (D) Photographs of isolated bilateral tumors. (E) Bilateral tumor volumes of mice after different formulations. (F) The weight of bilateral tumors. Representative FCM images of (G) $CD3^+CD4^+$ T cells in spleens, (H) $CD3^+CD8^+$ T cells in spleens, (I) $F4/80^+CD86^+CD206^-$ M1-like macrophage in tumors and (J) $F4/80^+CD86^-CD206^+$ M2-like macrophage in tumors. (K) CRT, HMGB1, cleaved Caspase 1 and GSDMD-N staining of tumor slices in different treatment groups. Scale bar: 100 μm. (L–R) Relative percentage of diverse immune cells treated differently. The data are displayed as mean ± SD and calculated by a Student's *t*-test. $^*P < 0.05$, $^{**}P < 0.01$, and $^{***}P < 0.001$.

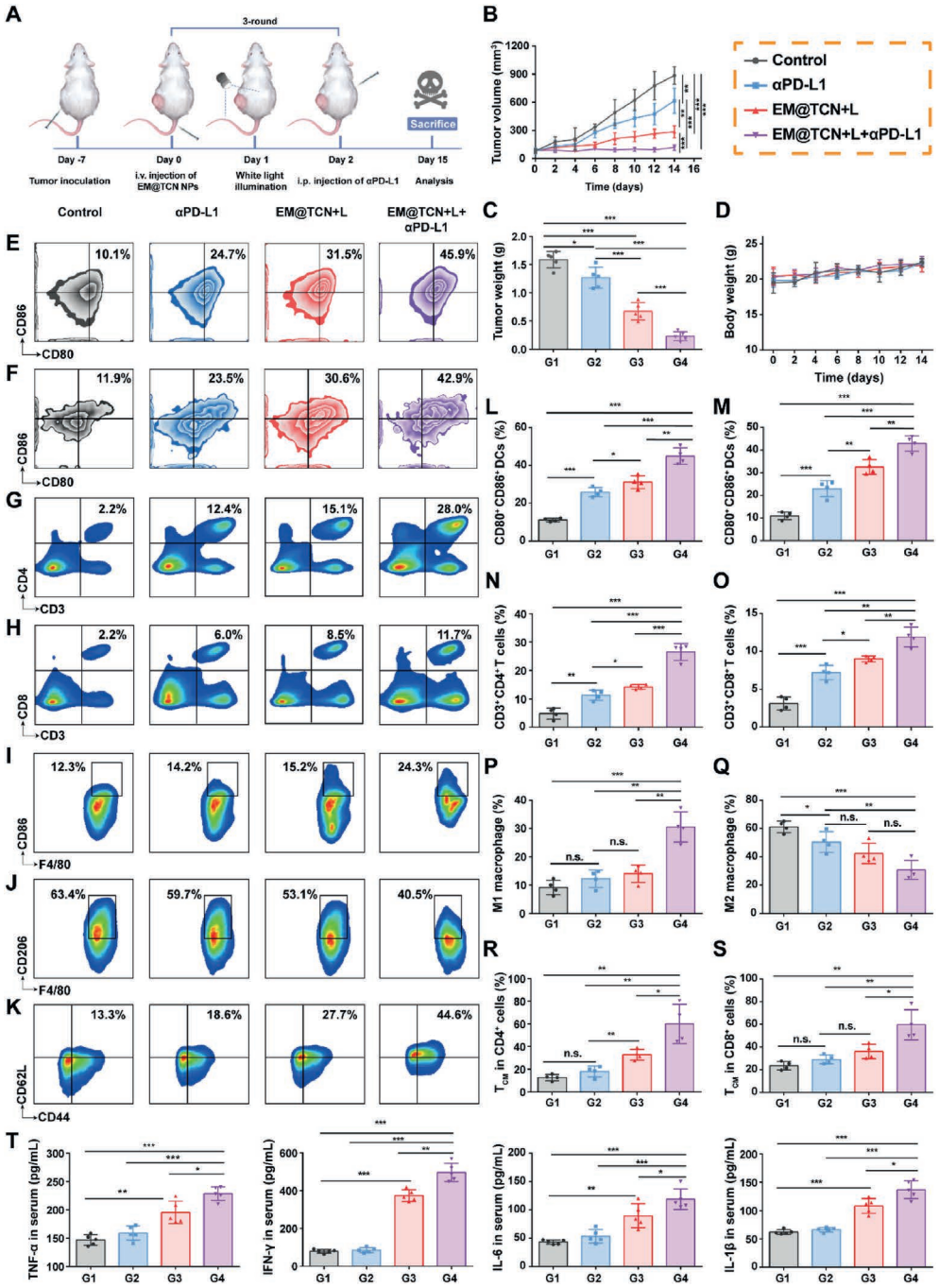

Figure 8 Antitumor effect combination with αPD-L1 in 4T1 subcutaneous tumor model. (A) Schematic illustration of the therapeutic strategy combined with αPD-L1 in subcutaneous 4T1-bearing-tumor mouse model. (B) Tumor volume growth curves of mice throughout the entire therapy period. (C) Tumor weight of excised tumors after different preparations. (D) Changes in body weight of mice among each group. Representative FCM images of (E) $CD80^+CD86^+$ DCs in spleens, (F) $CD80^+CD86^+$ DCs in tumors, (G) $CD3^+CD4^+$ T cells in spleens, (H) $CD3^+CD8^+$ T cells in spleens, (I) $F4/80^+CD86^+CD206^-$ M1-like macrophage in spleens, (J) $F4/80^+CD86^-CD206^+$ M2-like macrophage in spleens, and (K) $CD4^+CD44^+CD62L^+$ T_{CM} in spleens. (L–S) Relative percentage of diverse immune cells treated differently. (T) Cytokine including TNF-α, IFN-γ, IL-6 and IL-1β expression levels were detected in serum by ELISA assay kit. The data are displayed as mean ± SD and calculated by a Student's *t*-test. n.s.: no statistical significance, $^*P < 0.05$, $^{**}P < 0.01$, and $^{***}P < 0.001$.

treatments (Fig. 8D). To further explore the effect of EM@TCN + L + αPD-L1 on TME, serum, tumors and spleens were collected and investigated for related immune parameters. Firstly, the maturation of DCs were studied, as demonstrated in Fig. 8E and L, the proportions of $CD80^+CD86^+$ DCs were seen to be higher in EM@TCN + L + αPD-L1 group (45.9%) than in the Control group (10.1%) in spleens. In addition, Fig. 8F and M revealed that the percentages of $CD80^+CD86^+$ DCs treated with EM@TCN + L + αPD-L1 was 42.9%, which was 3.6 folds higher than Control group (11.9%) in tumors. Therefore, EM@TCN + L

combined with αPD-L1 could significantly induce DCs maturation. The antigens were presented to T cells and further trigger T-cell clone amplification after DCs matured[73]. As displayed in Fig. 8G and N, the ratios of $CD3^+CD4^+$ T cells apparently enhanced when the mice were treated with EM@TCN + L + αPD-L1 (28.0%), which was 12.7 folds higher than Control group (2.2%) in spleens, indicating that the combination of EM@TCN + L with αPD-L1 obviously increased T cells infiltration. The outcomes of $CD3^+CD8^+$ T cells had a similar tendency in spleens (Fig. 8H and O). Previous study has been proven that efficacious polarization of macrophages from M2-like to M1-like was able to facilitate tumor immunotherapy[74]. In comparation with the Control group, the ratios of $F4/80^+CD86^+CD206^-$ M1-like macrophage increased from 12.3% to 24.3%, and the ratios of $F4/80^+CD86^-CD206^+$ M2-like macrophage decreased from 63.4% to 40.5% after treatment with EM@TCN + L + αPD-L1 in the spleens (Fig. 8I, J, P and Q). To further evaluate the long-term immune memory of EM@TCN + L combined with αPD-L1, the expression of $CD4^+CD44^+CD62L^+$ or $CD8^+CD44^+CD62L^+$ T_{CM} in spleens were used to analyze the memory T cells. Obviously, EM@TCN + L + αPD-L1 treatment drastically increased the percentage of $CD8^+CD44^+CD62L^+$ or $CD4^+CD44^+CD62L^+$ T_{CM} than the other groups in spleens (Fig. 8K, R and S), indicating that a durable immune memory response could be triggered by EM@TCN + L + αPD-L1. Besides, the immune activity in the serum was also detected. The secretion of inflammatory cytokines was significantly increased such as TNF-α, IFN-γ, IL-6, IL-1β when the mice were treated with EM@TCN + L + αPD-L1, further indicating this therapeutic strategy could facilitate strong system immune response (Fig. 8T). In addition, there were no histopathological changes in major organs after diverse treatments were detected by H&E staining (Supporting Information Fig. S50). In conclusion, these outcomes demonstrated that a superior tumor ablation was achieved through the combination of EM@TCN + L with αPD-L1 in inhibiting subcutaneous 4T1-bearing-tumor model.

3.9. Combination antitumor effect of EM@TCN + L and αPD-L1 on 4T1 orthotopic tumor model and lung metastasis model

On the basis of the excellent antitumor effects of EM@TCN + L combined with αPD-L1 in subcutaneous 4T1-bearing-tumor mouse model, we next investigated the synergistic antitumor immune capability on orthotopic 4T1 tumor model. The mice were irregularly assigned into 4 groups, denoted as 1) Control, 2) αPD-L1, 3) EM@TCN + L, 4) EM@TCN + L + αPD-L1. The therapeutic strategy was illustrated in Fig. 9A. The growth of tumor volume was obviously suppressed in the group treated with EM@TCN + L + αPD-L1, in comparation with αPD-L1 or EM@TCN + L alone treated group, and there was no loss of mice body weight (Supporting Information Fig. S51). Obvious differences of tumors were observed in representative photos (Fig. 9B and C). Around 2 weeks later, after terminated the treatments, the tumors, spleens and tumor-draining lymph nodes (TDLNs) were harvested to assess the combined immunity responses by FCM. The matured DCs could stimulate antigen presentation and activate T cells[75]. As shown in Fig. 9D and H, EM@TCN + L + αPD-L1 treatment (29.5%) demonstrated the strongest capacity to promote DCs maturation in TDLNs, which was 3.0 folds higher than the Control group (9.7%). The similar trend was observed in the spleens and orthotopic tumors (Supporting Information Figs. S52 and S53). The percentages of $CD3^+CD4^+$ T cells levels in EM@TCN + L + αPD-L1 group (35.9%) were 3.8 folds higher than that in the Control group (9.4%) in tumors (Fig. 9E and I). Similarly, as Fig. 9F and J displayed, the proportions of $CD3^+CD8^+$ T cells of EM@TCN + L + αPD-L1 group was as high as 11.0%, which was about 3.5 folds compared with Control group (3.1%) in tumors. Subsequently, M1-like macrophages and M2-like macrophages were also investigated, which EM@TCN + L + αPD-L1 treatment could increase the M1-like macrophages ratios, with a decrease in the M2-like macrophages ratios, implying that EM@TCN + L + αPD-L1 could induce TAMs repolarization and reverse TME, further to initiate a better antitumor effect in the tumors (Supporting Information Fig. S54). Besides, EM@TCN + L + αPD-L1 treatment obviously enhanced the proportions of $CD8^+CD44^+CD62L^+$ T_{CM} from 14.0% to 58.9% compared with Control group in the tumors (Supporting Information Fig. S55). It is well known that immunosuppressive cells such as $CD4^+CD25^+$ Tregs plays an important part in impairing antitumor immunity and promote the rapid growth of tumor[76-78]. After treatment with EM@TCN + L + αPD-L1 (1.9%), the percentages of Tregs significantly decreased compared with Control group (16.8%) in spleens (Fig. 9G and K). In addition, immunofluorescence staining was also applied to detect the immune response in every group, which the outcomes were consistent with the FCM analysis. As depicted in Fig. 9L, the highest expression of $CD4^+$, $CD8^+$ and PD-L1 was observed in EM@TCN + L + αPD-L1 group compared with other treatment groups, which is of vital importance for pyroptosis induction and T cell-mediated systematic immune response compared with the other groups. Taken together, these above results solidly demonstrated that the combination with EM@TCN + L and αPD-L1 could significantly enhance the antitumor performance by powerfully initiating the pyroptosis-induced photoimmunotherapy and reshaping the immunosuppressive TME in orthotopic 4T1-bearing-tumor mouse model.

In view of the great tumor ablation and adaptive immunity *in vivo* initiated by EM@TCN + L + αPD-L1, we next established a lung metastasis model of breast cancer. In brief, when the tumor volumes became 50 mm^3, the mice were randomly divided into four groups: 1) Control, 2) αPD-L1, 3) EM@TCN + L, 4) EM@TCN + L + αPD-L1 groups. The administration protocol was depicted in Fig. 9M. On day 15, 4T1 cells were injected into the mice *via* the tail vein to form lung metastasis. After 30 days, mice were sacrificed to evaluate the antitumor performance of combination with EM@TCN + L and αPD-L1 in tumor therapy and lung metastasis inhibition. To assess the antitumor effect, the lungs of mice were harvested for further study. As Fig. 9N depicted, the number of pulmonary metastases in EM@TCN + L + αPD-L1 group exhibited apparently decline in comparation with the other groups. Besides, EM@TCN + L + αPD-L1 significantly suppressed the tumors growth and lung metastases, extended the survival period of mice, and no significant loss was observed in mice weight between diverse treatment groups, implying these formulations exhibited positive biosafety (Fig. 9O and P, Supporting Information Fig. S56). To investigate the underlying mechanism of EM@TCN + L + αPD-L1 treatment, the tumors and spleens were collected for FCM study. Firstly, as depicted in Fig. 9Q and Supporting Information Fig. S57A, EM@TCN + L + αPD-L1 (49.8%) could apparently enhance the ratios of matured $CD80^+CD86^+$ DCs compared with the Control group (3.8%) in tumors. The similar results were observed in the spleens, the percentages of $CD80^+CD86^+$ DCs in EM@TCN + L + αPD-L1 group was as high as 65.8%, which was 3.3 folds in

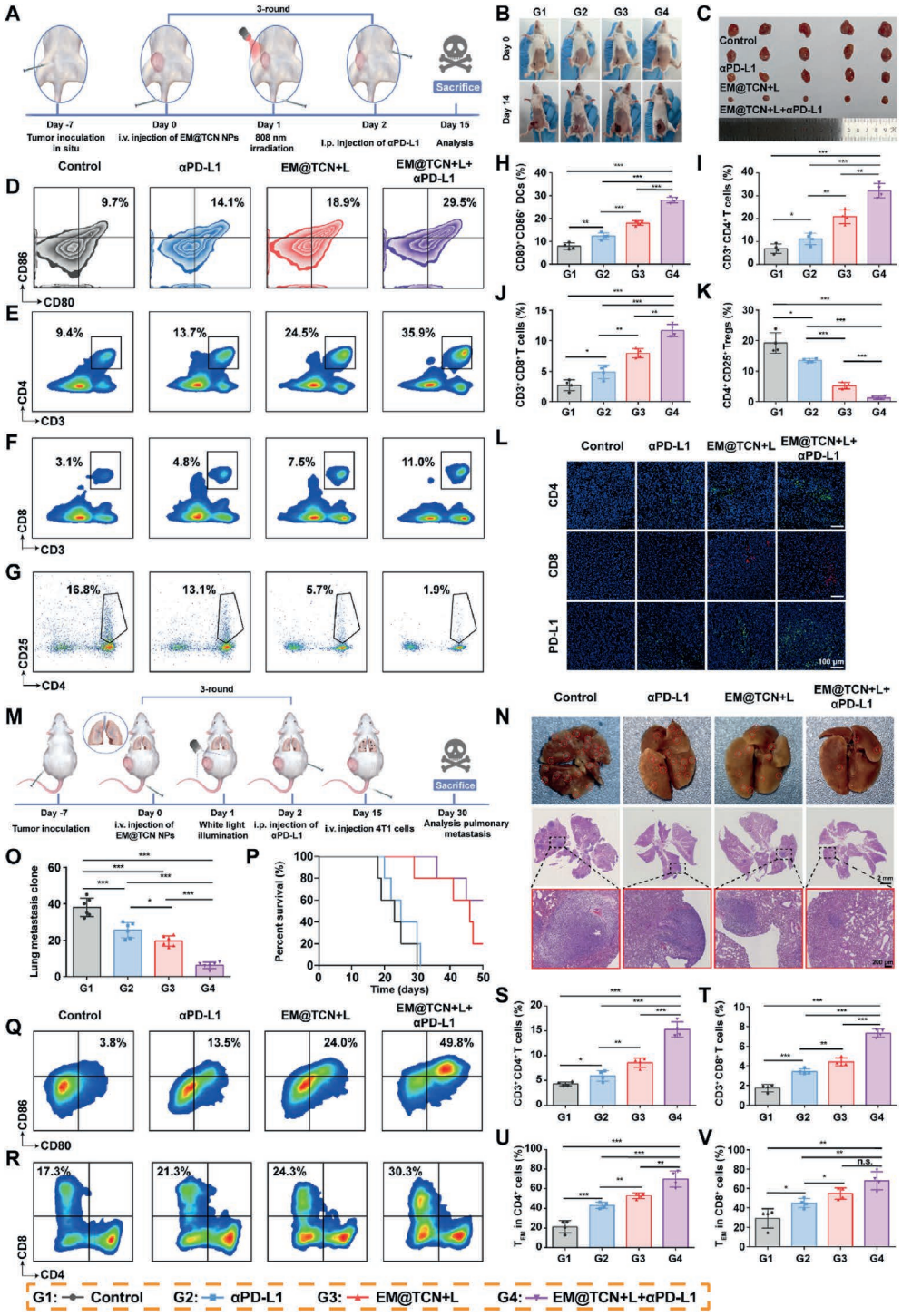

Figure 9 Antitumor effect combination with αPD-L1 in orthotopic 4T1 tumor model and 4T1 lung metastasis model. (A) Schematic illustration of the therapeutic strategy in orthotopic 4T1 tumor model. (B, C) Representative photographs of tumors in mice and excised tumors. Representative FCM images of (D) $CD80^+CD86^+$ DCs in TDLNs, (E) $CD3^+CD4^+$ T cells in tumors, (F) $CD3^+CD8^+$ T cells in tumors, (G) $CD4^+CD25^+$ Tregs in spleens. (H−K) Relative percentage of diverse immune cells treated differently. (L) CD4, CD8 and PD-L1 staining of tumor slices with various treatments. Scale bar: 100 μm. (M) Schematic diagram of the treatment in 4T1 lung metastasis model. (N) Representative photographs and H&E staining of isolated lung in diverse treatment groups. (O) Summary data of lung nodules. (P) Survive curves in each group. Representative FCM images of (Q) $CD80^+CD86^+$ DCs in tumors, (R) $CD8^+$ T cells in tumors. (S−V) Relative percentage of diverse immune cells treated differently. The data are displayed as mean ± SD and calculated by a Student's *t*-test. n.s.: no statistical significance, $^*P < 0.05$, $^{**}P < 0.01$, and $^{***}P < 0.001$.

comparation with Control group (19.9%) in the spleens (Supporting Information Fig. S58). As Fig. 9R and S57B displayed, the proportion of $CD3^+CD8^+$ T cells of EM@TCN + L + αPD-L1 group in tumors was 30.3%, which was 1.8 folds than that in the Control group (17.3%). Similarly, in comparation with the Control group, the proportions of $CD3^+CD4^+$ or $CD3^+CD8^+$ T cells increased obviously after treatment with EM@TCN + L + αPD-L1 in spleens (Fig. 9S and T and Supporting Information Fig. S59). In addition, the proportions of $F4/80^+CD86^+CD206^-$ M1-like macrophage and $F4/80^+CD86^-CD206^+$ M2-like macrophage in EM@TCN + L + αPD-L1 group was 24.9% and 19.7%, respectively, which was a 13.3% increase of M1-like macrophage and a 17.4% decline of M2-like macrophage compared with Control group in the tumors (Supporting Information Fig. S60). Besides, as depicted in Fig. 9U and V, EM@TCN + L + αPD-L1 treatments could obviously enhance the ratios of $CD4^+CD44^-CD62L^+$ or $CD8^+CD44^-CD62L^+$ T_{EM} in comparation with the Control group in tumors. The similar tendency of $CD4^+CD44^+CD62L^+$ or $CD8^+CD44^+CD62L^+$ T_{CM} was observed in tumors (Fig. S57C and S57D). In conclusion, above results strongly proved that EM@TCN + L + αPD-L1 could initiate system immune response and provoke a durable immunological memory response to inhibit tumor metastasis, accompanied by prolonged survival period of metastatic 4T1 tumor model.

All above experiments involving FCM gating strategies of immune cells *in vivo* were displayed in Supporting Information Figs. S61−S69.

4. Conclusions

In this work, we reported three homologous AIEgens with the identical backbone, named TMN, TBN and TCN, which was specifically anchoring to mitochondria, lysosome, and Golgi apparatus, respectively. Among three AIEgens, TCN exhibited strong emission, superior ROS production ability, good photostability, and negligible dark toxicity. To enhance the delivery efficacy of TCN, we designed a biomimetic hybrid EVs and M1-type macrophage membrane coated TCN (EM@TCN). Notably, EM@TCN plus white light irradiation could induce a specific pyroptosis process executed by GSDM family and the release of cellular contents such as pro-inflammatory cytokines and immunostimulatory components, eventually lead to the release of DMAPs and TAA. Of note, the occurrence of pyroptosis in EM@TCN plus white light irradiation during PDT not only supported by the morphological and mechanistic characteristics, but also validated by the subsequent comprehensive transcriptome sequencing analysis. *In vitro* cellular experiments indicated that EM@TCN plus white light irradiation can significantly inhibit the 4T1 cells migration and invasion, enhance the exposure of CRT and the release of HMGB1 transform nuclear to cytoplasm, lead to the DCs maturation. *In vivo* animal experiments indicated that EM@TCN plus white light irradiation could effectively reshape the TME by enhancing DCs maturation, promoting the cytotoxic T lymphocytes infiltration and alleviating immunosuppression environment, thereby boosting T cell-mediated systematic immune response, eventually demonstrated to be favorable eradication primary tumors but also inhibition distant tumor. In addition, combining EM@TCN + L with immune checkpoint blockade therapies (αPD-L1) can significantly enhance the immunogenicity of the tumor and inhibit the subcutaneous and orthotopic breast tumor growth, particularly in elimination of 4T1 tumor metastasis. As far as we know, this is the first report of GA-targeted AIE photosensitizer to induce pyroptosis and enhancing antitumor pyroptotic photoimmunotherapy combined with ICB. These findings pave the ways to develop more efficient biometric nanoplatforms, precise light-controlled and traceable subcellular localization AIE probe through subtle structural modification to instruct fluorescence imaging-based PDT and antitumor immunity.

Acknowledgments

This work was financially supported by National Natural Science Foundation of China (No. 32070356). We would like to thank Xiaonan Ma for providing technical assistance of confocal microscopy work on the Public Experimental Platform of China Pharmaceutical University (Nanjing, China). Moreover, the authors thank Dr. Hui-Min Xu of the Public Laboratory Platform at China Pharmaceutical University for assistance with NMR techniques. All animal experiments were performed in accordance with the Guidelines for Care and Use of Laboratory Animals of China Pharmaceutical University and agreed with the Institutional Animal Ethics Committee of China Pharmaceutical University (SYXK2021-0010).

Author contributions

Xing Zhao conceived the project and designed the experiment. Ninghua Tan and Huachao Chen provided financial support and supervision. Xing Zhao, Xi Wu, Ranran Shang and Haitao Dou were responsible for conducting experiments and analyzing data. Xing Zhao wrote the manuscript and it was revised by Ninghua Tan and Huachao Chen.

Conflicts of interest

The authors declare no conflict of interest.

Appendix A. Supporting information

Supporting information to this article can be found online at https://doi.org/10.1016/j.apsb.2025.11.010.

References

1. Ribas A, Wolchok JD. Cancer immunotherapy using checkpoint blockade. *Science* 2018;**359**:1350−5.
2. Sharma P, Hu-Lieskovan S, Wargo JA, Ribas A. Primary, adaptive, and acquired resistance to cancer immunotherapy. *Cell* 2017;**168**:707−23.
3. Andrews LP, Yano H, Vignali DAA. Inhibitory receptors and ligands beyond PD-1, PD-L1 and CTLA-4: breakthroughs or backups. *Nat Immunol* 2019;**20**:1425−34.
4. O'Donnell JS, Teng MWL, Smyth MJ. Cancer immunoediting and resistance to T cell-based immunotherapy. *Nat Rev Clin Oncol* 2019; **16**:151−67.
5. Hugo W, Zaretsky JM, Sun L, Song C, Moreno BH, Hu-Lieskovan S, et al. Genomic and transcriptomic features of response to anti-PD-1 therapy in metastatic melanoma. *Cell* 2016;**165**:35−44.
6. Hegde PS, Chen DS. Top 10 challenges in cancer immunotherapy. *Immunity* 2020;**52**:17−35.
7. Irvine DJ, Hanson MC, Rakhra K, Tokatlian T. Synthetic nanoparticles for vaccines and immunotherapy. *Chem Rev* 2015;**115**:11109−46.

8. Liu X, Xia S, Zhang Z, Wu H, Lieberman J. Channelling inflammation: gasdermins in physiology and disease. *Nat Rev Drug Discov* 2021;**20**:384−405.
9. Song X, Huang H, Xia L, Jia W, Yang S, Wang C, et al. Engineering 2D multienzyme-mimicking pyroptosis inducers for ultrasound-augmented catalytic tumor nanotherapy. *Adv Sci* 2023;**10**:2301279.
10. Broz P, Pelegrín P, Shao F. The gasdermins, a protein family executing cell death and inflammation. *Nat Rev Immunol* 2020;**20**:143−57.
11. Wu D, Wang S, Yu G, Chen X. Cell death mediated by the pyroptosis pathway with the aid of nanotechnology: prospects for cancer therapy. *Angew Chem Int Ed* 2021;**60**:8018−34.
12. Humphries F, Shmuel-Galia L, Ketelut-Carneiro N, Li S, Wang B, Nemmara VV, et al. Succination inactivates gasdermin D and blocks pyroptosis. *Science* 2020;**369**:1633−7.
13. Wang K, Sun Q, Zhong X, Zeng M, Zeng H, Shi X, et al. Structural mechanism for GSDMD targeting by autoprocessed caspases in pyroptosis. *Cell* 2020;**180**:941−55.
14. Shi J, Zhao Y, Wang K, Shi X, Wang Y, Huang H, et al. Cleavage of GSDMD by inflammatory caspases determines pyroptotic cell death. *Nature* 2015;**526**:660−5.
15. Ding J, Wang K, Liu W, She Y, Sun Q, Shi J, et al. Pore-forming activity and structural autoinhibition of the gasdermin family. *Nature* 2016;**535**:111−6.
16. Xu K, Chang M, Wang Z, Yang H, Jia Y, Xu W, et al. Multienzyme-mimicking $LaCoO_3$ nanotrigger for programming cancer-cell pyroptosis. *Adv Mater* 2023;**35**:2302961.
17. Wang H, Gao Z, Jiao D, Zhang Y, Zhang Z, Wang T, et al. A microenvironment dual-responsive nano-drug equipped with PD-L1 blocking peptide triggers immunogenic pyroptosis for prostate cancer self-synergistic immunotherapy. *Adv Funct Mater* 2023;**33**:2214499.
18. Ding B, Chen H, Tan J, Meng Q, Zheng P, Ma P, et al. ZIF-8 nanoparticles evoke pyroptosis for high-efficiency cancer immunotherapy. *Angew Chem Int Ed* 2023;**62**:e202215307.
19. Li J, Anraku Y, Kataoka K. Self-boosting catalytic nanoreactors integrated with triggerable crosslinking membrane networks for initiation of immunogenic cell death by pyroptosis. *Angew Chem Int Ed* 2020;**59**:13526−30.
20. Li M, Kim J, Rha H, Son S, Levine MS, Xu Y, et al. Photon-controlled pyroptosis activation (PhotoPyro): an emerging trigger for antitumor immune response. *J Am Chem Soc* 2023;**145**:6007−23.
21. Li Z, Mo F, Wang Y, Li W, Chen Y, Liu J, et al. Enhancing gasdermin-induced tumor pyroptosis through preventing ESCRT-dependent cell membrane repair augments antitumor immune response. *Nat Commun* 2022;**13**:6321.
22. Ling YY, Xia XY, Hao L, Wang WJ, Zhang H, Liu YL, et al. Simultaneous photoactivation of cGAS-STING pathway and pyroptosis by platinum(II) triphenylamine complexes for cancer immunotherapy. *Angew Chem Int Ed* 2022;**61**:e202210988.
23. Su W, Qiu W, Li SJ, Wang S, Xie J, Yang QC, et al. A dual-responsive STAT3 inhibitor nanoprodrug combined with oncolytic virus elicits synergistic antitumor immune responses by igniting pyroptosis. *Adv Mater* 2023;**35**:2209379.
24. Wang Q, Wang Y, Ding J, Wang C, Zhou X, Gao W, et al. A bio-orthogonal system reveals antitumour immune function of pyroptosis. *Nature* 2020;**579**:421−6.
25. Baguley BC. Multiple drug resistance mechanisms in cancer. *Mol Biotechnol* 2010;**46**:308−16.
26. Fan JX, Deng RH, Wang H, Liu XH, Wang XN, Qin R, et al. Epigenetics-based tumor cells pyroptosis for enhancing the immunological effect of chemotherapeutic nanocarriers. *Nano Lett* 2019;**19**:8049−58.
27. Lucky SS, Soo KC, Zhang Y. Nanoparticles in photodynamic therapy. *Chem Rev* 2015;**115**:1990−2042.
28. Li X, Lee D, Huang JD, Yoon J. Phthalocyanine-assembled nanodots as photosensitizers for highly efficient type I photoreactions in photodynamic therapy. *Angew Chem Int Ed* 2018;**57**:9885−90.
29. Wu W, Mao D, Hu F, Xu S, Chen C, Zhang CJ, et al. A highly efficient and photostable photosensitizer with near-infrared aggregation-induced emission for image-guided photodynamic anticancer therapy. *Adv Mater* 2017;**29**:1700548.
30. Wang SP, Huang X, He Y, Zhang H, Zhou J, Tang G, et al. Amphiphilic porphyrin-based supramolecular self-assembly for photochemotherapy: from molecular design to application. *Nano Today* 2023;**48**:101732.
31. Zhao X, Liu J, Fan J, Chao H, Peng X. Recent progress in photosensitizers for overcoming the challenges of photodynamic therapy: from molecular design to application. *Chem Soc Rev* 2021;**50**:4185−219.
32. Kang M, Zhang Z, Song N, Li M, Sun P, Chen X, et al. Aggregation-enhanced theranostics: AIE sparkles in biomedical field. *Aggregate* 2020;**1**:80−106.
33. Shi L, Wu W, Duan Y, Xu L, Xu L, Hou X, et al. Light-induced self-escape of spherical nucleic acid from endo/lysosome for efficient non-cationic gene delivery. *Angew Chem Int Ed* 2020;**59**:19168−74.
34. Feng G, Liu B. Aggregation-induced emission (AIE) dots: emerging theranostic nanolights. *Acc Chem Res* 2018;**51**:1404−14.
35. Hu F, Xu S, Liu B. Photosensitizers with aggregation-induced emission: materials and biomedical applications. *Adv Mater* 2018;**30**:1801350.
36. Wang BW, Jiang K, Li JX, Luo SH, Wang ZY, Jiang HF, et al. 1,1-Diphenylvinylsulfide as a functional AIEgen derived from the aggregation-caused-quenching molecule 1,1-diphenylethene through simple thioetherification. *Angew Chem Int Ed* 2019;**59**:2338−43.
37. Mei J, Leung NLC, Kwok RTK, Lam JWY, Tang BZ. Aggregation-induced emission: together we shine, united we soar. *Chem Rev* 2015;**115**:11718−940.
38. Yu K, Ye B, Yang H, Xu X, Mao Z, Zhang Q, et al. A mitochondria-targeted NIR-II AIEgen induced pyroptosis for enhanced tumor immunotherapy. *Adv Healthcare Mater* 2023;**12**:2301693.
39. Wu M, Liu X, Chen H, Duan Y, Liu J, Pan Y, et al. Activation of pyroptosis by membrane-anchoring AIE photosensitizer design: new prospect for photodynamic cancer cell ablation. *Angew Chem Int Ed* 2021;**60**:9093−8.
40. Chen H, Luo X, Huang Q, Liu Z, Lyu M, Chen D, et al. Platelet membrane fusion liposome loaded with type I AIE photosensitizer to induce chemoresistance cancer pyroptosis and immunogenic cell death for enhancing cancer immunotherapy. *Chem Eng J* 2023;**476**:146276.
41. Wang M, Wu M, Liu X, Shao S, Huang J, Liu B, et al. Pyroptosis remodeling tumor microenvironment to enhance pancreatic cancer immunotherapy driven by membrane anchoring photosensitizer. *Adv Sci* 2022;**9**:2202914.
42. Deng C, Zhao X, Chen Y, Ai K, Zhang Y, Gong T, et al. Engineered platelet microparticle-membrane camouflaged nanoparticles for targeting the Golgi apparatus of synovial fibroblasts to attenuate rheumatoid arthritis. *ACS Nano* 2022;**16**:18430−47.
43. Luo J, Zhang P, Zhao T, Jia M, Yin P, Li W, et al. Golgi apparatus-targeted chondroitin-modified nanomicelles suppress hepatic stellate cell activation for the management of liver fibrosis. *ACS Nano* 2019;**13**:3910−23.
44. Zhao X, Wu X, Shang RR, Chen HC, Tan NH. A structure-guided strategy to design Golgi apparatus-targeted type-I/II aggregation-induced emission photosensitizers for efficient photodynamic therapy. *Acta Bio* 2024;**183**:235.
45. Lai JJ, Chau ZL, Chen SY, Hill JJ, Korpany KV, Liang NW, et al. Exosome processing and characterization approaches for research and technology development. *Adv Sci* 2022;**9**:2103222.
46. Zheng C, Zhong Q, Yi K, Kong H, Cao F, Zhuo C, et al. Anti−phagocytosis-blocking repolarization-resistant membrane-fusogenic liposome (ARMFUL) for adoptive cell immunotherapy. *Sci Adv* 2023;**9**:eadh2413.
47. Rodell CB, Arlauckas SP, Cuccarese MF, Garris CS, Li R, Ahmed MS, et al. TLR7/8-agonist-loaded nanoparticles promote the polarization of tumour-associated macrophages to enhance cancer immunotherapy. *Nat Biomed Eng* 2018;**2**:578−88.
48. Xing X, Jia Y, Zhang J, Wu Z, Qin M, Li P, et al. A novel aggregation induced emission (AIE) fluorescence probe by combining

tetraphenylethylene and 2′,3′-*O*-isopropylideneadenosine for localizing Golgi apparatus. *Sens Actuators, B* 2021;**329**:129245.
49. Chen LB. Mitochondrial membrane potential in living cells. *Annu Rev Cell Dev Biol* 1988;**4**:155−81.
50. Xu W, Lee MMS, Nie JJ, Zhang Z, Kwok RTK, Lam JWY, et al. Three-pronged attack by homologous far-red/NIR AIEgens to achieve 1+ 1+ 1> 3 synergistic enhanced photodynamic therapy. *Angew Chem Int Ed* 2020;**59**:9610−6.
51. Liu M, Chen Y, Guo Y, Yuan H, Cui T, Yao S, et al. Golgi apparatus-targeted aggregation-induced emission luminogens for effective cancer photodynamic therapy. *Nat Commun* 2022;**13**:2179.
52. Elias EE, Lyons B, Muruve DA. Gasdermins and pyroptosis in the kidney. *Nat Rev* 2023;**19**:337−50.
53. Liu Y, Zhen W, Wang Y. $Na_2S_2O_8$ nanoparticles trigger antitumor immunotherapy through reactive oxygen species storm and surge of tumor osmolarity. *J Am Chem Soc* 2020;**142**:21751−7.
54. Li M, Kim J, Xu Y. An acid-activatable nanosensitizer library realizes tunable pyroptosis activation in tumors. *Matter* 2023;**6**: 15−8.
55. Nakamura N, Lowe M, Levine TP, Rabouille C, Warren G. The vesicle docking protein p115 binds GM130, a cis-Golgi matrix protein, in a mitotically regulated manner. *Cell* 1997;**89**:445−55.
56. Eisenberg-Lerner A, Benyair R, Hizkiahou N, Nudel N, Maor R, Kramer MP, et al. Golgi organization is regulated by proteasomal degradation. *Nat Commun* 2020;**11**:409.
57. Kayagaki N, Stowe IB, Lee BL, O'Rourke K, Anderson K, Warming S, et al. Caspase-11 cleaves gasdermin D for non-canonical inflammasome signalling. *Nature* 2015;**526**:666−71.
58. Liu X, Zhang Z, Ruan J, Pan Y, Magupalli VG, Wu H, et al. Inflammasome-activated gasdermin D causes pyroptosis by forming membrane pores. *Nature* 2016;**535**:153−8.
59. Chen X, He W, Hu L, Li J, Fang Y, Wang X, et al. Pyroptosis is driven by non-selective gasdermin-D pore and its morphology is different from MLKL channel-mediated necroptosis. *Cell Res* 2016;**26**: 1007−20.
60. Aglietti RA, Estevez A, Gupta A, Ramirez MG, Liu PS, Kayagaki N, et al. GsdmD p30 elicited by caspase-11 during pyroptosis forms pores in membranes. *Proc Natl Acad Sci USA* 2016;**113**:7858−63.
61. Xia S, Zhang Z, Magupalli VG, Pablo JL, Dong Y, Vora SM, et al. Gasdermin D pore structure reveals preferential release of mature interleukin-1. *Nature* 2021;**593**:607−11.
62. Tang Y, Bisoyi HK, Chen XM, Liu Z, Chen X, Zhang S, et al. Pyroptosis-mediated synergistic photodynamic and photothermal immunotherapy enabled by a tumor-membrane-targeted photosensitive dimer. *Adv Mater* 2023;**35**:2300232.
63. Tang L, Yin Y, Cao Y, Fu C, Liu H, Feng J, et al. Extracellular vesicles-derived hybrid nanoplatforms for amplified CD47 blockade-based cancer immunotherapy. *Adv Mater* 2023;**35**:2303835.
64. Ding J, Lu G, Nie W, Huang LL, Zhang Y, Fan W, et al. Self-activatable photo-extracellular vesicle for synergistic trimodal anticancer therapy. *Adv Mater* 2021;**33**:2005562.
65. Ma H, Fang W, Li Q, Wang Y, Hou SX. Arf1 ablation in colorectal cancer cells activates a super signal complex in DC to enhance antitumor immunity. *Adv Sci* 2023;**10**:2305089.
66. Pittet MJ, Michielin O, Migliorini D. Clinical relevance of tumour-associated macrophages. *Nat Rev Clin Oncol* 2022;**19**:402−21.
67. Togashi Y, Shitara K, Nishikawa H. Regulatory T cells in cancer immunosuppression−implications for anticancer therapy. *Nat Rev Clin Oncol* 2019;**16**:356−71.
68. Ding M, Zhang Y, Yu N, Zhou J, Zhu L, Wang X, et al. Augmenting immunogenic cell death and alleviating myeloid-derived suppressor cells by sono-activatable semiconducting polymer nanopartners for immunotherapy. *Adv Mater* 2023;**35**:2302508.
69. Bronte V, Brandau S, Chen SH, Colombo MP, Frey AB, Greten TF, et al. Recommendations for myeloid-derived suppressor cell nomenclature and characterization standards. *Nat Commun* 2016;**7**:12150.
70. Wang J, Wang J, Hong W, Zhang L, Song L, Shi Q, et al. Optineurin modulates the maturation of dendritic cells to regulate autoimmunity through JAK2-STAT3 signaling. *Nat Commun* 2021;**12**:6198.
71. Shi W, Feng W, Li S, Cui Y, Liu S, Jiang H, et al. Ferroptosis and necroptosis produced autologous tumor cell lysates co-delivering with combined immnoadjuvants as personalized *in situ* nanovaccines for antitumor immunity. *ACS Nano* 2023;**17**:14475−93.
72. Xiao Y, Zhang T, Ma X, Yang QC, Yang LL, Yang SC, et al. Microenvironment-responsive prodrug-induced pyroptosis boosts cancer immunotherapy. *Adv Sci* 2021;**8**:2101840.
73. Long Y, Fan J, Zhou N, Liang J, Xiao C, Tong C, et al. Biomimetic Prussian blue nanocomplexes for chemo-photothermal treatment of triple-negative breast cancer by enhancing ICD. *Biomaterials* 2023;**303**: 122369.
74. Choo YW, Kang M, Kim HY, Han J, Kang S, Lee JR, et al. M1 macrophage-derived nanovesicles potentiate the anticancer efficacy of immune checkpoint inhibitors. *ACS Nano* 2018;**12**:8977−93.
75. Choi Y, Lichterman JN, Coughlin LA, Poulides N, Li W, Del Valle P, et al. Immune checkpoint blockade induces gut microbiota translocation that augments extraintestinal antitumor immunity. *Sci Immunol* 2023;**8**:eabo2003.
76. Malfitano AM, Pisanti S, Napolitano F, Di Somma S, Martinelli R, Portella G. Tumor-associated macrophage status in cancer treatment. *Cancers* 2020;**12**:1987.
77. Zhang L, Song A, Yang QC, Li SJ, Wang S, Wan SC, et al. Integration of AIEgens into covalent organic frameworks for pyroptosis and ferroptosis primed cancer immunotherapy. *Nat Commun* 2023;**14**:5355.
78. Overacre-Delgoffe AE, Chikina M, Dadey RE, Yano H, Brunazzi EA, Shayan G, et al. Treg-mediated Iimmunosuppression in tumor progression. *Cell* 2017;**169**:1130−42.